MARTIN MARIETTA ENERGY SYSTEMS LIBRARIES
3 4456 0365960 9

2

ORNL-3486
UC-34 – Physics
TID-4500 (21st ed.)

# THE PRINCIPLES AND MEASUREMENT OF FISSION-FRAGMENT TIMES OF FLIGHT

(Thesis)

W. F. Mruk

CENTRAL RESEARCH LIBRARY
DOCUMENT COLLECTION
LIBRARY LOAN COPY
DO NOT TRANSFER TO ANOTHER PERSON
If you wish someone else to see this document, send in name with document and the library will arrange a loan.

OAK RIDGE NATIONAL LABORATORY
operated by
UNION CARBIDE CORPORATION
for the
U.S. ATOMIC ENERGY COMMISSION

LEGAL NOTICE

This report was prepared as an account of Government sponsored work. Neither the United States, nor the Commission, nor any person acting on behalf of the Commission:

A. Makes any warranty or representation, expressed or implied, with respect to the accuracy, completeness, or usefulness of the information contained in this report, or that the use of any information, apparatus, method, or process disclosed in this report may not infringe privately owned rights; or

B. Assumes any liabilities with respect to the use of, or for damages resulting from the use of any information, apparatus, method, or process disclosed in this report.

As used in the above, "person acting on behalf of the Commission" includes any employee or contractor of the Commission, or employee of such contractor, to the extent that such employee or contractor of the Commission, or employee of such contractor prepares, disseminates, or provides access to, any information pursuant to his employment or contract with the Commission, or his employment with such contractor.

ORNL-3486

Contract No. W-7405-eng-26

INSTRUMENTATION AND CONTROLS DIVISION

# THE PRINCIPLES AND MEASUREMENT OF FISSION-FRAGMENT TIMES OF FLIGHT

W.F. Mruk

(Submitted as a thesis to the Graduate Council of The University of Tennessee in partial fulfillment of the requirements for the degree of Doctor of Philosophy)

DATE ISSUED

8-29-63

OAK RIDGE NATIONAL LABORATORY
Oak Ridge, Tennessee
Operated by
UNION CARBIDE CORPORATION
for the
U.S. ATOMIC ENERGY COMMISSION

MARTIN MARIETTA ENERGY SYSTEMS LIBRARIES
3 4456 0365960 9

## ACKNOWLEDGEMENTS

The author is indebted to Dr. C.J. Borkowski for his encouragement and sustained interest in this project, to Dr. H.W. Schmitt, who stimulated the experiment, and to Dr. R.W. Lide, whose discussions proved extremely valuable.

Thanks are due to Mr. R.H. Ward for his clever mechanical designs in the apparatus and to Dr. J.H. Neiler and Mr. H.N. Wilson for many discussions on electronics.

TABLE OF CONTENTS


| CHAPTER | | PAGE |
|---|---|---|
| I. | INTRODUCTION | 1 |
| II. | THEORY | 7 |
| III. | APPARATUS | 9 |
| | Physical Description | 9 |
| | Flight Tubes | 9 |
| | Vacuum Systems | 9 |
| | Electronic Systems | 10 |
| | Detectors | 12 |
| | Zero Time Detector | 12 |
| | Foil Preparation | 14 |
| | Transducers | 16 |
| | Remote Detectors | 17 |
| | Signal Processing | 19 |
| | Fast Timing Signals | 19 |
| | Cable Calibration | 20 |
| | Time-to-Pulse-Height Converter | 25 |
| | Description | 25 |
| | Description of Operation | 26 |
| | Adjustment Procedure | 27 |
| | Procedural Limitations with Delay Cables | 29 |
| | Procedural Limitations with Detectors | 30 |
| | Differential Linearity | 35 |

CHAPTER PAGE

IV. TIME-TO-PULSE-HEIGHT CONVERTER SIGNAL PROCESSING . . . . . 39

Signal Characteristics . . . . . 39

Drift and Gain Stability . . . . . 41

V. SLOW CHANNEL . . . . . 43

Signal Characteristics . . . . . 43

Coincidence Constraints and Characteristics . . . . . 43

VI. ANALYSIS OF THE EXPERIMENTAL TIME MEASUREMENT . . . . . 46

Detector Transit Times . . . . . 46

Velocity Expressions . . . . . 49

The Effects of Prompt Neutron Emission . . . . . 55

VII. PRECISION OF THE EXPERIMENT . . . . . 59

Precision Indices of the Apparatus . . . . . 59

Precision Indices Due to Effects of Prompt Neutron Emission . . . . . 59

Corrections . . . . . 60

Best Estimate of Precision of Velocity Measurement . . 61

VIII. CONCLUSIONS . . . . . 65

Detector Improvements . . . . . 65

Circuit Improvements and Criteria . . . . . 67

BIBLIOGRAPHY . . . . . 69

REFERENCES . . . . . 70

APPENDIXES

A. ANALYSIS OF THE TPHC OUTPUT CIRCUITRY . . . . . 72

APPENDIXES PAGE

B. THE DISTRIBUTION OF TIME INTERVALS FORMED BETWEEN A FIXED-FREQUENCY PULSER AND A RANDOM TIME SOURCE AS MEASURED BY THE TPHC . . . . . 77

C. CHANCE COINCIDENCE RATES IN A TRIPLE COINCIDENCE SYSTEM . . . . . 82

D. FIGURES . . . . . 87

# LIST OF FIGURES


| FIGURE | | PAGE |
|---|---|---|
| 1. | Schematic Diagram of Time-of-Flight Apparatus | 87 |
| 2. | Typical Vacuum Station | 88 |
| 3. | Instrumentation and Controls Diagram for Vacuum Stations | 89 |
| 4. | Block Diagram of the Time-of-Flight Electronics System | 90 |
| 5. | Schematic Diagram of the White Cathode-Follower Pre-Amplifier | 91 |
| 6. | Schematic Diagram of Modified Pulse-Height Selector of a Standard A-1 Amplifier | 92 |
| 7. | Time Sequence of the Pulses in the Double Time-of-Flight Apparatus | 93 |
| 8. | Zero Time Detector | 94 |
| 9. | Foil Processor | 95 |
| 10. | Typical Remote Detector | 96 |
| 11. | Detector Voltage Divider Network | 97 |
| 12. | Schematic Diagram for Measuring Cable Delay Time | 98 |
| 13. | Standard Cable Terminator | 99 |
| 14. | Resultant Waveshapes in Cable Calibrations | 100 |
| 15. | Time-to-Pulse-Height Converter | 101 |
| 16. | Photographs of Typical Diode-Stretcher Voltage Shapes in the Time-to-Pulse-Height Converter | 102 |
| 17. | Time-of-Flight Spectrum for $Pu^{239}$ | 103 |
| 18. | Digital Plot of Figures 17a, b, and c to Establish the Validity of the ART Effect | 104 |

FIGURE PAGE

19. Differential Linearity of the 0-2 Side of the TPHC . . . . . 105

20. Einzel Lens of the Zero Time Detector . . . . . 106

21. Salient Parameters for Determining the Correlated Fission-Fragment Velocities from the Measurement of Correlated Fission-Fragment Flight Times . . . . . 107

22. Time-of-Flight Spectra . . . . . 108

# CHAPTER I

## INTRODUCTION

Evidence for the existence of fission was first established by radiochemical methods by Hahn and Strassman[1,2] in 1939. Traditionally much of the succeeding work in fission, particularly the investigations on the mass distribution, has been done in radiochemistry[3,4] and mass-spectrography.[5] Mass yields from the fission of $U^{233}$, $U^{235}$, and $Pu^{239}$, investigated by radiochemical and mass-spectrometric methods, have been recently summarized by Katcoff,[6] who tabulated "best values" obtained by these methods.

Early measurements of the kinetic parameters, particularly the kinetic energy, of the fission fragments were done with ionization chambers.[7,8,9] Frisch[7] first confirmed the large energy release accompanying fission by recording the large pulses of ionization produced in a gas chamber by fission fragments.[10] These measurements were followed by energy measurements performed calorimetrically by Henderson,[11] and later by Leachman and Schafer.[12]

Brunton and Hanna,[8] and Brunton and Thompson,[9] using double ionization chambers, were able in principle to make correlated energy measurements from which a fragment mass distribution could be determined, and obtained other correlations of kinetic parameters of the fission process.

Unfortunately, significant discrepancies occurred between the results reported for these various experiments. One such discrepancy is the lower average kinetic energy of the fragments reported by the ionization chamber method than by the calorimetric method. Another discrepancy

occurs in the comparison between the mass distributions obtained radiochemically and those obtained by the ionization chamber method. The ionization chamber method shows that the fission fragment mass distribution peaks are wider and further separated than those determined radiochemically, in each instance by more than the experimental uncertainties.[13]

In an effort to reconcile these discrepancies, Leachman[14] introduced the time-of-flight method in order to obtain a directly measured distribution of fission fragment velocities. From these data, he obtained values for total kinetic energy in agreement with the calorimetric results. He also showed that the fission fragment velocity distributions calculated from the energy data obtained with ionization chambers were in disagreement with his results by evaluating the displacement in velocity between the peaks in the two distributions in terms of the energy-ionization ratios of fission fragments. From the energy-ionization ratios determined by the time-of-flight method, and applied as a correction to the ionization chamber data, he was able to show good agreement between the data obtained with the calorimetric and the ionization chamber methods for the average total kinetic energy of the fission fragments. The ionization chambers in the early experiments were initially calibrated with alpha particles of known energy and then used to measure the relative ionization produced by the fission fragments. Knipp and Ling[15] had suggested that the discrepancy in the results between the radiochemical method and the ionization chamber method lay in an "ionization defect." Indeed such a defect was experimentally established by Schmitt and Leachman,[16] and Leachman and Schmitt,[17] who showed that fission fragments stopped in a gas expend larger averages of

energy per ion pair formed than alpha particles stopped in the same gas; hence, the ionization defect.

A natural extension to the time-of-flight method was to measure the velocity of both fragments in a double drift-tube apparatus[18,19] analogous to the double, or back-to-back, ionization chamber apparatus. Thus, correlated velocity measurements could now be made. Such measurements are more satisfactory and straightforward because they are characterized by lower dispersions than energy measurements and because the ionization defect is absent. Furthermore, since the time-of-flight measurements permit the mass ratio of the fragments to be determined from a velocity ratio rather than from an energy ratio, the inherent dispersion due to neutron emission in the mass ratio determined from time-of-flight experiments is one-half the corresponding dispersion by the ion chamber method. Specifically, in the case of velocity measurements, the conservation equations yield:

$$M_1^* v_1^* = M_2^* v_2^*; \tag{1}$$

$$M_1^* + M_2^* = A + 1, \tag{2}$$

where: $M_{1,2}^*$ = pre-prompt neutron emission fission fragment mass,

$v_{1,2}^*$ = pre-prompt neutron emission fission fragment velocity,

$A$ = mass number of fissile nucleus,

$1$ = in amu, the increase in mass number of A due to absorption of one thermal neutron.

For a given mass split, and a given value of $v_1^*$ and $v_2^*$, the final average velocity of the fragment is:

$$< v_i > \; = \; v_i^*; \qquad i \; = \; 1,2. \tag{3}$$

Here, the average is formed over all emitted neutron directions and energies based on the assumption that the neutrons are emitted isotropically in the center-of-mass coordinate system attached to each fragment.

Equations (1) and (2) yield, for $M_1^*$:

$$M_1^* \; = \; \frac{A + 1}{1 + \frac{v_1}{v_2}}, \tag{4}$$

or

$$M_2^* \; = \; \frac{A + 1}{1 + \frac{v_2}{v_1}}. \tag{5}$$

From the uncertainties in the velocity measurements, the uncertainty in the masses described by Equations (4) and (5) is about one and one-half amu.

For the case of correlated energy measurements, the conservation equations yield:

$$m_1^* E_1^* \; = \; m_2^* E_2^*,$$

where: $E_1^*$, $E_2^*$ are the pre-prompt neutron emission fission fragment kinetic energies.

In analogy with Equation (3),

$$< E_i > \; = \; E_i^* \frac{m_i}{m_i^*}; \qquad i \; = \; 1,2. \tag{6}$$

Therefore, for any event, the determination of $m_i^*$ depends specifically on the number of neutrons emitted for a given mass split and kinetic energy

division. This function, expressed as $\gamma(m_i, E_i^*)$ is not known in all the required detail; hence, the estimated accuracy in measuring $m_i^*$ from the energy-correlated experiments is about ± 2 amu, and the dispersion due to neutron emission is about another one and one-half amu.

More recently, Milton and Fraser[20] and others[21] have reported more refined data obtained with elaborate time-of-flight apparatus on $U^{233}$, $U^{235}$, $Pu^{239}$, and $Cf^{252}$. However, with the advent of solid-state detectors, which again are energy measuring devices, significant discrepancies have reappeared between time-of-flight and energy correlated data.

Time-of-flight methods not only yield information on velocity determinations and mass distribution, but also can be profitably extended to include magnetic analysis, wherein the mass-to-charge ratios of the fission fragments lead to smaller errors in mass determinations and to possible correlations between pre- and post-neutron emission masses. Further extensions of these methods can correlate velocity and energy measurements, leading to detailed examination of the kinetic parameters of the fission process. The feasibility of these extensions provided a strong motivation to pursue time-of-flight measurements at the Oak Ridge National Laboratory based on the existence of a research reactor capable of producing sufficient flux to make such advanced experiments possible.

To this end, a double time-of-flight apparatus for fission fragments has been assembled at the Oak Ridge Research Reactor. In the course of assembling and testing this apparatus, a number of measurement problems of a fundamental nature have appeared. Detailed investigations of these problems have proved necessary for the determination of the accuracy and

precision of the measurements and for the development of satisfactory techniques, at each step in the experiment, for performing the measurement. It is the purpose of this research, therefore, to establish the precision with which the correlated flight times of the fission fragments can be measured with this specific apparatus, to establish qualitatively and quantitatively the limitations of the apparatus, and to investigate and analyze in as much detail as possible the fundamental physical effects which are important in these measurements.

# CHAPTER II

## THEORY

Basically, the time-of-flight measurement is a velocity determination. In the present case, the velocities of fission fragment pairs formed by thermal neutron induced fission are derived from a measurement of their correlated flight times over known path lengths.

Because the fragment flight times are in the hundreds of nanoseconds ($10^{-9}$ sec = 1 nsec) time domain and difficult to process electronically, they are first transformed into voltage pulses whose amplitudes are proportional to flight times. The voltage pulses are subsequently transformed back to the μsec time domain via a pulse-height-to-time converter utilizing the standard lengthener, ramp generator, comparator, and oscillator count-down technique.[28]

A minimum of three signals must be employed for the measurement of correlated flight times; viz., a zero-time signal which heralds a specific fission event, and two remote signals which announce the arrival of the sister fragments at the ends of their respective flight paths. The zero-time signal is delayed for a time slightly longer than the longest flight time expected, so what is really measured are the supplements of the flight times, labeled appropriately, the measured times.

To insure that the signals heralding the zero of time and the end-of-flight times are legitimate, a constraint in the form of a triple coincidence is placed upon the timing signals. The timing signals are derived from the anodes of fourteen-stage photomultipliers; whereas, the signals

for the triple coincidence constraint are derived from the tenth dynodes of the same photomultipliers.

# CHAPTER III

# APPARATUS

## A. Physical Description

### 1. Flight Tubes

The time-of-flight apparatus consists of two cylindrical 2S aluminum tubes, one-eighth inch thick, diametrically opposed and connected to the zero-time detector box. The entire assembly is oriented vertically with respect to the Oak Ridge Research Reactor thermal neutron beam hole, HB1 (See Figure 1). The flight path extending from the source of fissionable material in the zero box to the uppermost of #2 detector is labeled 0-2; whereas, the flight path extending downward to the #1 detector is labeled 0-1. The 0-1 flight tube attached to the bottom of the zero box has an inner diameter of six inches; the 0-2 flight tube attached to the top of the zero box varies in diameter over three sections. The first section, adjacent to the zero box, is six inches I.D., the next section is ten inches I.D., and the third section furthest from the zero box is twelve inches I.D. This design feature made it possible to detect and account for the fission fragments rendered non-colinear by recoil from prompt-neutron emission. The 0-2 flight path is 343.84 ± 0.08 cm long; the 0-1 flight path, 301.15 ± 0.08 cm long.

### 2. Vacuum Systems

The assembly of flight tubes and zero box is evacuated to a nominal pressure of $2 \times 10^{-6}$ mm Hg via vacuum ports located near each remote detector. Two nominally independent dynamic vacuum systems are

used to evacuate the assembly (See Figure 2). Because the vacuum assembly is large and directly couples both vacuum pumping systems, elaborately instrumented pumping stations were devised to protect against cracking the diffusion pump oil and/or inadvertently exposing the cold trap to pressures greater than $10^{-3}$ mm Hg (See Figure 3).

## B. Electronic Systems

### 1. Basic Description

Figure 4 is a block diagram of the electronic components used in timing the flights of the fission fragments and in effecting the triple coincidence constraint. The normal sequence of events starts when a thermal neutron from the ORR induces fission in the source located at zero. The source itself consists of a nickel foil nominally $3 \times 10^{-6}$ in. thick onto which is evaporated fissile material to a thickness of about $100 \times 10^{-6}$ gm/cm$^2$. It is oriented so that the fissile material faces detector #1. With such an arrangement, a fission fragment headed for detector #1 proceeds unhindered in its flight while its sister fragment must pass through two nickel foils. The first foil is the source backing; the second, located five and one-half inches above, and parallel to, the source, serves as a source of delta rays - ejected by the sister fragment as it passes through the foil while enroute to detector #2. The delta rays are electrostatically focused onto a thin plastic phosphor, or scintillator,* 0.0005 in. thick which is optically coupled to a light pipe

---

*NE102 purchased from Nuclear Enterprises Ltd., Winnepeg, Manitoba.

and a 6810-A photomultiplier tube. Two output signals are extracted from this tube: a negative one from the anode which serves as the zero-of-time signal, and a positive one from the tenth dynode which serves as one of the three necessary coincidence signals. The negative signal is delayed 633.95 ± 0.025 nsec which is a time about 100 nsec longer than the longest fragment flight time anticipated.

After passing through the foils, the fragment continues up the 0-2 drift tube at the end of which it is detected by a two inch diameter thin plastic scintillator 0.001 in. thick coupled to a 6810-A photomultiplier through a two inch diameter, one-fourth inch quartz light pipe. The scintillator is bonded to the quartz with a bonding agent.* The complementary fragment proceeds down the 0-1 flight tube at the end of which it encounters a similarly constructed detector. Both remote detectors provide timing and coincidence signals comparable with those of the zero detector.

The timing signals, which are fast pulses, are introduced directly into the time-to-pulse-height converter via 50 ohm accurately time-calibrated cables.** In contrast, the slow, or time-coincident, signals are first amplified by standard linear-amplifier pre-amplifiers modified with White cathode-follower output circuits (See Figure 5). These slow signals are further amplified by standard A-1 linear amplifiers whose pulse-height selector output circuitry has been redesigned to produce negative,

---

*R823, R.A. Biggs Company.

**Andrews Heliax HO cable, manufactured by the Andrews Cable Att. = 1.6 db/1000 ft at $10^9$ cps.

variable time duration, fixed-amplitude rectangular pulses. It is these rectangular pulses which serve as triggers to the coincidence circuitry (See Figure 6).

Meanwhile, the outputs of the time-to-pulse-height converter are amplified by pre-amplifiers identical to the one described above, and then further amplified by standard A-1 amplifiers. The A-1 amplifiers produce output pulses of uniform shape whose amplitudes are proportional to the measured-time intervals.

Figure 7 is a graphical analysis of the pulse sequence used to measure the flight times of the fission fragments and how their validity is established via the coincidence constraint.

## C. Detectors

### 1. Zero Time Detector

Figure 8 shows the detailed arrangement of the zero time detector. The basic design for this detector was developed by Stein and Leachman.[22] In this experiment, both the fissile source and delta ray Ni foils are oriented at $45^{\circ}$ to the drift tube axis but parallel to each other. Both foils are 0.068 $mg/cm^2$ or 3 $\mu$in. thick. In order to reduce the neutron beam attenuation through the aluminum source holder, a wedge-shaped adaptor plate was inserted between the source holder and lens structure. In this way, the fissile source is exposed directly to the neutron beam with a negligible change in angle with respect to the delta ray foil. Because a fission fragment is a highly charged particle (of the order of 20 electron charges),[23] delta rays are promptly emitted from both surfaces of a foil as the fragment traverses it. The number of delta particles

formed varies at the square of the charge of the traversing fragment;[24] they escape from depths of no more than a few micrograms per square centimeter in the foil.[44] The number of electrons ejected from foils of nickel, aluminum, copper, silver, and gold is 70 within 10% for fragments emerging from the foils.[22] Further measurements by Stein and Leachman showed: (1) the efficiency for detecting $U^{235}$ fission fragments by this method is greater than 95%, with a 95% confidence limit and (2) the velocity loss through 0.1 mg/cm$^2$ nickel foils was less than 1%. It is safe therefore to state that the velocity loss through the foils of this experiment for $U^{235}$ fission fragments is also less than 1%; hence, negligible changes in direction of the detected fragments resulted.

Measurements[22] with a 4.8 mev alpha source showed that the average number of electrons emitted was approximately two. Similar measurements in this experiment indicated an upper limit of two consistent with these results; thus, this type of detector exhibits excellent alpha particle rejection ability. Based on a known pulse height response to fission fragments, the relative response to alpha particles was estimated at between one and two electrons.

The NE102 scintillator used as the transducer in the zero detector was covered with a similar 0.068 mg/cm$^2$ nickel foil which served as a light reflector and as a zero-potential equipotential surface. This equipotential surface kept the electric field generated by the applied lens voltage from diverging in the region of the scintillator, and thus improved the focusing properties of the einzel lens.

2. Foil Preparation

The fissile material backing and delta ray source are thin metallic foils* of nickel 3 μin. thick. The nickel is initially evaporated onto a relatively thicker and stronger copper foil. This procedure renders the composite foils tractable until the nickel foil itself is needed. To this end, the copper portion of the composite foil is removed chemically. A machine especially designed and constructed for handling the foils during the processing is shown in Figure 9. At all times, the nickel foils are moved slowly and oriented such that the normal to the foil surface is at a right angle with respect to the direction of motion.

The composite foils are first cemented, copper side free, with a dilute solution of glyptal** to an aluminum holder one inch by one inch with a three-fourth inch diameter hole. A locating pin is fashioned to one corner of the holder. It serves a second purpose in preventing the foils from lying flat (as they are placed in storage prior to use) when air entrained beneath them can cause them to burst. Care is exercised in applying the glyptal so that none of it extends beyond the holder onto the free surface of the nickel. The different expansion coefficients between the glyptal and nickel can result in tearing the foil while it is drying after processing.

---

*Purchased from the Chromium Corporation of America, Waterbury, Conn.

**Purchased from the General Electric Corp., #7815.

The chemical used to dissolve the copper from the nickel selectively is a chromic acid solution. It is prepared by first making a saturated solution of chromium trioxide ($CrO_3$) in distilled water and then adding 15 cc of concentrated sulphuric acid per 1000 cc of solution.

The aluminum holder with the composite foil cemented to it is attached to arms "A" of the Foil Processor with set screws. Two 450 ml beakers containing the chromic acid are placed into position beneath the holders, and motor "M" is energized through switch "S" placed in the "Insert" position. The holders are driven at the rate of approximately one-half in. per minute into the chromic acid until they are completely immersed. The motor drive is then stopped by limit switch "L.S.I." No further insertion is possible. After being immersed in the chromic acid for thirty minutes the copper is usually dissolved leaving the 3 μin. nickel foil on the holder. With switch "S" placed in the withdraw position, motor "M" is again energized but drives in the reverse direction until limit switch "L.S.W." is reached. Withdraw motion ceases and both nickel foils are clear of the chromic acid beakers. These beakers are then removed and replaced by two similar beakers now filled with a 25% solution of distilled water and 180 proof ethyl alcohol. The foils are driven into and out of this solution where they are rinsed clean of any residual chromic acid. They are removed from arms "A" immediately after the withdraw limit switch is reached and are directly placed in compartmentalized plastic boxes to dry in a reasonably dust-free atmosphere. Dust particles settling on wet foils resulted in their drying unevenly and produced wrinkles on their surfaces. Such wrinkling affected the source deposit uniformity as well as the delta ray source thickness

resulting in a variable energy loss as the fragments passed through. It also affected the ultimate strength and life of the foils due to the production of high internal stresses in the wrinkles.

3. Transducers

NE102, a phosphor impregnated plastic furnished by the Nuclear Enterprises Ltd., Winnepeg, Manitoba, served as the basic transducer in all detectors. The manufacturer lists the decay constant at $4 \times 10^{-9}$ seconds with a scintillation response to electrons 60% that of an anthracene crystal of the same weight. Two thicknesses of NE102 were used: the zero detector used a 0.0005 in. thickness; the #2 and #1 detectors, a 0.001 in. thickness. The motivation for using thin scintillators lay in reducing the gamma ray background in all three detectors. The zero detector is located in a particularly hostile environment since it is located almost directly in the reactor beam.

Obviously, the scintillators are not self-supporting, particularly against a differential pressure equal to atmospheric across them; hence, the need for light pipers. The minimum piper thickness was set by the tensile strength of the piper material. The maximum piper thickness was limited by the material light absorption characteristics. To this end, the piper material selected was quartz, one-fourth in. thick, and one and three-fourths in. in diameter.

The NE102 was bonded to the quartz with the R.A. Biggs Co. bonding agent R823. The bonding agent was diluted with the recommended hardener and a thin coating of the solution applied to the quartz with a brush. The solution remained untouched on the quartz for about five minutes. During this time, air bubbles entrained in the solution worked their way

out under the influence of gravity. Next, the NE102 was laid on the bonding solution, and the air trapped between the bonding solution and scintillator was rolled out with an aluminum rolling-pin three-fourth in. in diameter. A twenty-four hour curing period at room temperature then followed, after which the excess NE102 and cured bonding agent were cut away from the quartz with an Exacto knife.

4. Remote Detectors

The detectors signaling the end-of-flight of the fragments are labeled #2 and #1 (See Figure 4). Each detector consists of a primary transducer -- the NE102 scintillator described under Transducers -- bonded to a two in. diameter, one-quarter in. thick quartz light pipe coupled with vacuum grease to an RCA 6810-A fourteen stage photomultiplier (See Figure 10). A peripheral "O" ring vacuum seals the quartz light pipe against the aluminum structure of the flight tubes. The photomultiplier itself presses against the vacuum grease and quartz through the action of spacer springs compressed by wing nuts, WN. The photomultiplier light shield anchors each detector to the flight tubes at its respective location.

It was found that phenolic photomultiplier tube bases contained radioactive material* and were characterized by electrical leakages between pins when voltage was applied to the photomultiplier tube. This condition contributed greatly to the background noise of the detector. To combat this noise problem, the photomultiplier tube bases were machined from Teflon and the voltage divider networks were soldered pin-to-pin.

---

*P.R. Bell, private communication, 1963.

Figure 11 represents the detector voltage divider network. Since the detectors were to be used in a very low light level, low noise, high-gain service, the resistor values shown in Figure 11 were selected in accordance with the manufacturer's recommendations.* Furthermore, because regenerative phenomena contribute to the noise at higher voltages, the maximum voltage applied to the divider string was 2.1 kilovolts. The optimum value of voltage was determined experimentally; conjointly, the focusing and accelerating electrode voltages were varied and set at the values corresponding to the maximum output signal.

A serious limitation to the reliability of the detector systems lay in the coupling capacitors C10 and C13. Originally these were glass enclosed, oil filled capacitors.** It was necessary to use these capacitors because of the potential gradients developed across them. However, the leads of these capacitors did not seal the dielectric fluid within the glass envelope reliably; consequently, the fluid would leak out at the junction of the lead and capacitor envelope. Although the dielectric loss played havoc with the tube base by insulating the base pins from the photomultiplier pins, the more important effect was that the loss of dielectric fluid was accompanied by the admission of water vapor into the envelope. The water vapor did not affect the capacity values particularly but was responsible for an appreciable noise build-up. Since this action was slow in time, the noise build-up was insidious. Rather than study the

---

*RCA Electron Tube Division, Data Sheet 6810-A 11-58.

**Dearborn Electric Company, Type GTL 37L103.

effect in detail, it was more expedient simply to clean the base pins with a solvent (Metriclene*) and replace the capacitors. Before using any of the detectors for a run, a systematic check of the noise background was made, referenced to the noise level of the detector when it was first installed (and the noise level minimal). Later, the Dearborn capacitors were replaced by a comparable unit, hermetically sealed and completely covered with an Epoxy resin.**

## D. Signal Processing

### 1. Fast Timing Signals

The fast signals derived from the anodes of the 6810-A photomultiplier tubes are transmitted to the time-to-pulse-height converter via appropriate lengths of the Andrews Heliax Type HO coaxial cable. The nominal characteristic impedance of the cable is fifty ohms. Its attenuation factor is listed at 1.6 db per 1000 feet at 1000 megacycles. Its dispersion will be discussed in the following section in which the cable time delay calibration is presented. To aid in stabilizing its characteristics, the cable is pressurized with dry nitrogen at greater than 10 psi gauge.

Two lengths of HO cable each twenty-five feet long coupled the remote detector signals to the "Start" inputs of the time-to-pulse-height converter. The "Stop" signal derived from the zero detector fast output was delayed through 540 feet of this same type cable. Since the primary

---

*Metriclene purchased from the J.B. Moore Company.

**Sprague Electric Company.

timing information is contained in the difference in times of arrival of the Start and Stop pulses, the time delays introduced by the cables must be known to an accuracy of better than 0.1%. The reason for this demand will be discussed under Cable Calibration.

2. Cable Calibration

Several considerations arise in measuring the time delays of the type HO cables as well as the cables used for calibrating the apparatus. One consideration centers about the type of calibrating signal used. Will cables calibrated with continuous sine waves yield results consonant with results derived from pulsed calibrating signals? Or should the calibrating signals be comparable with the signals derived from the detectors? These considerations are burning questions in the nanosecond region because the wavelengths associated with these frequencies are small compared with the circuit dimensions. Actually cable dispersion distorts the shape of the calibrating pulses; hence, it is imperative that the cables be calibrated with pulses exactly as those delivered by the detectors. In the extreme, the calibrating pulses should at least have the same rise time as the detector signals. Gatti and Svelto[25] show that if a length of cable having delay "r" is not matched at both ends, but has a total reflection coefficient $\rho = \rho_1\rho_2$, where $\rho_1$ and $\rho_2$ are the reflection coefficients at the two ends, it gives an output pulse whose centroid is delayed by:

$$t_{ct.d} = r\,\frac{1 + \rho}{1 - \rho}, \tag{7}$$

with respect to the input centroid.

For the principal mode transmission along coaxial cables, Maxwell's equations yield:

$$\rho_A = \frac{Z_A - Z_o}{Z_A + Z_o}, \tag{8}$$

where: $\rho_A$ = voltage reflection coefficient,

$Z_A$ = impedance connected across an end of the line,

$Z_o$ = characteristic impedance of the line.

For the case $Z_A = Z_o$, $\rho_A = 0$, there is no reflected wave and all the power is absorbed in the pure resistance $Z_o$. Such a line is said to be matched.

For the case $Z_A = 0$, corresponding to a short circuit, $\rho_A = -1$. The reflected voltage wave is of the same amplitude as the incident one but opposite in sign. For any other case, however, it is difficult to see what is meant by Equation (7); e.g., consider the case $Z_A = nZ_o$ where $n \neq 0$.

$$\rho_A = \frac{(n - 1)\, Z_o}{(n + 1)\, Z_o}, \tag{9}$$

or $$\rho_A = \frac{n - 1}{n + 1};$$

then, $$\rho = \rho_1\rho_2 = \left(\frac{n - 1}{n + 1}\right)^2,$$

and $$t_{ct.d} = r\frac{1 + \rho}{1 - \rho} \text{ becomes:} \tag{10}$$

$$\frac{t_{ct.d}}{r} = \frac{1 + (\frac{n - 1}{n + 1})^2}{1 - (\frac{n - 1}{n + 1})^2},$$

$$= \frac{1}{2}(n + \frac{1}{n}).$$

which states that for large and small values of n there are large delays in the pulse centroid.

The validity of Equation (10) was investigated experimentally during the calibrating procedure described in the next paragraph. Within the limits of the experimental uncertainty of the calibration procedure ($\epsilon < 0.5\%$), no such shifts in pulse centroids were observed.

In any event, the two extreme termination cases and the considerations bearing on the phase distortion and amplitude attenuation of the calibrating pulses led to the following technique for calibrating the delay lines. A continuous series of regular, constant amplitude, five nsec rise-time square wave pulses were sent down a given delay cable. The far end of the cable was short circuited. The incident pulses were reflected but reversed in sign and returned to the driven end of the cable. The frequency of the pulses was varied until a reflected pulse and a subsequent incident pulse overlapped and cancelled each other. (It is tacitly assumed that the pulse duration is much shorter than the cable delay time.) When this condition accrued, the frequency of the pulses was equal to the reciprocal of twice the cable delay time; i.e., the round trip time of the pulses. Note that a cancellation can occur at harmonic frequencies; however, it was a simple matter to determine the fundamental frequency by starting at a very low frequency and sweeping to higher ones. The first interference pattern identified itself readily.

The measurement is executed in the manner shown in Figure 12. The Tektronix Type 105 square wave generator was used as the source of calibrating pulses. The rise time of these pulses was less than 20 nsec with the generator set to its 1 Mc/sec range. Because the pulses are generated by a flip-flop and are subject to the "walk" and drift inherent in such circuitry, it was necessary to set the square wave generator near the correct frequency and to synchronize it with a sine wave (General Radio Company Model 1211B) oscillator. The output of the square wave generator is terminated with the manufacturer's "L" pad. The cable to be calibrated is connected to one arm of the "T" fitting on the output side of the termination. A Tektronix Model 517 oscilloscope is connected to the other arm of the "T" and serves as the visual indicator for the condition of cancellation. When the optimum cancellation is achieved as viewed by the oscilloscope, the frequency of the pulses is digitally counted by a Beckman/Berkeley Model 7175 frequency counter. The accuracy of this device is plus or minus one cycle in 100 megacycles. To minimize all problems of loading the cable system under measurement, the synchronized output of the square wave generator is utilized for two purposes: (1) to synchronize the oscilloscope and (2) to drive the frequency counter. At the condition of optimum cancellation at the driven end of the cable, there is barely enough residual voltage to energize the oscilloscope let alone to drive the frequency counter.

It is observed that the reflected pulse differs from the incident pulse in that:

1) the rise time of the reflected pulse is longer than that of the incident pulse.

2) the amplitude of the reflected pulse is smaller than that of the incident pulse.

3) the time duration of the reflected pulse is slightly longer than that of the incident pulse.

4) the incident pulse sharper rise time generates some small ringing.

Observations (1) and (3) are accounted for by attributing dispersive properties to the line; (2) to the line attenuation and (4) to the fact that the line is shock excited by the incident pulse.

Note that Gatti's criterion, Equation (7), is of little consequence with this technique, for the far end of the line is terminated with a zero impedance while the driven end is terminated in its characteristic impedance.

The question of terminating impedance always arises with transmission lines and particularly so in the nanosecond region where the wavelength of the transmitted electromagnetic radiation is of the order of the circuit and transmission line dimensions. A length of wire considered as a wire-over-ground transmission line represents about 3.3 nh/cm of inductance and 1/3 pf/cm of capacitance with a characteristic impedance somewhere between 50 and 200 ohms -- these values being the limits of impedance physically realizable.[26,27] Assuming a value of 100 ohms for the transmission line impedance, a 50 ohm coaxial cable terminated with a 50 ohm resistor with 2 cm leads has an $\frac{L}{R}$ time constant of 50 psec. (There is a 100 ohm loop impedance in the cable.) If the criterion to be met is that the correct termination be established to 1% in 0.5 nsec, there are 20 time constants available to reach 99% of steady state.

To insure that even this slight deviation in termination be minimized in calibrating the zero-time delay cable, the argument presented in the preceding paragraph was carried to the limit by reducing the characteristic impedance of the "short circuit." This reduction is accomplished by paralleling the shirt-circuiting wire indefinitely; the limit is a disc type resistor of zero ohms. A conveniently constructed disc short is shown in Figure 13.

Figure 14a shows a graphical study of the oscilloscope patterns expected in effecting the optimum cancellation of the calibrating pulses. Figure 14b is a sequence of photographs showing the actual oscilloscope patterns obtained.

Table I lists the experimental values of the frequencies measured in calibrating the zero-time delay cable. Five different observers were used in setting the frequency by oscilloscope observation. They consistently agreed to within less than ± 0.3 Kc in 788.7 Kc. Assuming the deviations are normally distributed, the value assigned to the zero-time delay cable is $T_D = 633.95 \pm 0.025$ nsec.

The measured values and precisions of the time delays of the 2-FS and 1-FS cables are:

2-FS = 25.62 ± 0.035 nsec;

1-FS = 25.46 ± 0.035 nsec.

## E. Time-To-Pulse-Height Converter

### 1. Description

The heart of the time-of-flight apparatus is the time-to-pulse-height converter, hereafter referred to as the TPHC. It is through this

instrument that the transfer from the nanosecond time domain to pulse height takes place (See Figure 15); these pulse heights are then transformed back to the microsecond region via a pulse-height-to-time converter utilizing the standard lengthener, ramp generator, comparator, and oscillator countdown technique.[28]

The particular instrument to be described is comparable with a circuit reported by Beghian, based on an original design by J.H. Neiler.[29] It differs from Beghian's in that a single Stop pulse is used to define the end-of-range time for two separate but correlated Start pulses. For purposes of discussion, consider a single side of the TPHC consisting of but one remote detector and the zero-time detector.

2. Description of Operation

A Start pulse generated at a remote detector anode is applied to the grid of V1 via the twenty-five feet of type HO cable. V1 is a 404A pentode, a vacuum tube whose grid is gold-plated to reduce secondary emission and is located very close to the cathode to provide high (12,500 $\mu$ mhos) transconductance. The fast rise time ($\sim 2 \times 10^{-9}$ sec) of the signal from the remote detector cuts off tube V1 in a time essentially shorter than that of the thirty nanosecond shorted delay line located in the plate circuit of V1. This impulse charges the stray capacitance at the grid of V4 via diode D1. The voltage step remains trapped until a negative Stop pulse from the anode of the zero-time detector arrives at the grid of V3 via the zero-time delay cable. The Stop pulse is inverted by V3 and delivers a positive pulse to the grid of V2 whose plate current discharges the signal trapped between diodes D1 and D2. If no Stop pulse

appears, the trapped signal leaks off through the reverse resistance of the trapping diodes.

A diode, D4, holds the cathode of V4 essentially at ground potential. As the grid of V4 is driven positive via the positive trapped signal, its cathode potential rises slightly, cuts off diode D4, and diverts the diode current through V4.

At the same time, the tube current is held constant by the large cathode resistance tied to the 150 volts negative supply, and capacitor $C_2$ is discharged linearly at a constant rate; thus:

$$\int_{t'=0}^{t'=t} dV_c = \frac{1}{C_2} \int_{t'=0}^{t'=t} I\, dt'. \tag{11}$$

At I = constant,

$$V_c(t) - V_c(0) = \frac{I}{C_2} t.$$

Let: $V_c(t) - V(0) = \Delta V_c.$

Then, $$\Delta V_c = \left(\frac{I}{C_2}\right)t. \tag{12}$$

Both the capacitor value and current are constant; hence, the voltage change across the capacitor is linear with time and directly proportional to it. Since the capacitor has been charged during the interval between the arrival of the Start and Stop pulses, the potential developed across it is a measure of this time interval.

3. Adjustment Procedure

There are three major controls in the TPHC. Potentiometer R1 (Figure 15) controls the bias of the dump tube V3. Potentiometer R3 controls the bias of the constant current tube V4, while potentiometer R5

limits the current through V4 and hence determines the slope of the discharge voltage across $C_2$ [See Equation (4)].

With too little bias on V3, the diode-stretcher is discharged by the quiescent current of V3 in a time shorter than the maximum fragment flight-time; consequently, the diode-stretcher voltage pulse duration will not be a measure of fragment flight-time. The diode-stretcher voltage corresponding to this condition is shown in Figure 16.

With too large a bias on V3, the Stop pulses inverted by V0 and applied to the grid of V3 are incapable of driving V3 into conduction; again, the diode-stretcher voltage pulse duration will not be a measure of fragment flight-time. The diode-stretcher voltage persists for times dependent on the reverse diode resistance and diode-stretcher capacitance. These times are a factor of 40-50 longer than the maximum fragment-flight-times.

The optimum bias setting on V3 corresponds to the situation where the decrease in the diode-stretcher voltage is essentially zero over 633.95 nsec which is slightly greater than the maximum anticipated fragment flight-time and is equal to the Stop pulse cable delay time.

The optimum bias setting of V4 occurs when V4 is just cut off. Then for any positive voltage on the diode-stretcher, V4 begins to conduct, the potential at the cathode of V4 rises and quickly cuts off diode D4. In this mode of operation, the plate current of V4 is relatively constant and its value dependent on R, $R_L$, and $R_P$ (See Appendix I). Since the plate current of V4 determines the slope of the discharge voltage developed across $C_2$ [See Equation (4)], it follows that this slope is dependent on the setting of R which exceeds the values of $(R_L + R_P)$ by a factor of 10

and is therefore the dominant resistance factor.

The TPHC is initially calibrated with delay cables, themselves previously calibrated by the technique described under Cable Calibration. A mercury pulser furnishes fast rise-time pulses each of which is divided and transmitted through lengths of delay-cable whose time delay differences simulate fission fragment flight times.

4. Procedural Limitations with Delay Cables

Electrical and electronic effects which are generally negligible in the microsecond time domain become limitations in the nanosecond time domain because the wavelengths of the electromagnetic phenomena associated with the nanosecond time domain are of the same size as the circuit dimensions. Pulses with rise times of a few nanoseconds are treated as square-wave pulses in microsecond circuitry but can render timing errors when such pulses are used to define time intervals in the nanosecond time domain. Therefore, several limitations to calibrating the TPHC with external delay cables and a mercury pulser must be considered.

The mercury pulser signals are unequally attenuated by the different lengths of delay cables used in forming the time differences. This unequal attenuation produces a walk in the time at which the TPHC input tubes are cut off. The assumption is made here that the pulse amplitude is sufficient to cut off these tubes. For the case where the pulse attenuation is so great that the input circuits are not completely cut off, it is evident that the variance in the arrival times of the centroids of the pulser signals and consequently in the "machine time" is greater than in the former case. Here "machine time" is defined as the time

during which V4, the constant current tube of the TPHC, conducts and thereby defines the simulated flight time. This effect depends on the absolute magnitude of the pulser signals and whether the TPHC input circuitry is sensitive to the centroid of the used fraction of pulser signal or to the centroid of the total integral of the pulser signal.[30]

The second limitation of this calibration lies in the calibrating signals. These signals are derived from a mercury pulser but suffer degradation in rise time as they are attenuated. The reactive components in resistors, switches, and associated wiring of the mercury pulser are not negligible at the very high frequencies corresponding to pulse rise times of one or two nanoseconds; hence variations in the rise times of the calibrating signals introduce timing errors due to "walk."

The two aforementioned limitations combine to accentuate a second-order effect, viz., a walk error based on diode-stretcher voltage-amplitude variations. Even so, the timing resolution is still less than 1.5 nsec, FWHM.

5. Procedural Limitations with Detectors

Basically, the same limitations associated with calibrating the TPHC with the mercury pulser are still present when the detectors are substituted for the pulser but with three additions.

First, because the number of excited states formed in the scintillator depends upon the mass and the energy of the specific fission fragment, the number of photons accompanying the decay of these excited states and the subsequent emission of photoelectrons from the photocathode of the photomultiplier tube also strongly depend upon the particular incident fragment. On the average, the amplitude of the output pulses from the

photomultiplier ranges over a factor of approximately two to one for fission fragments incident on the same spot of the scintillator.

Secondly, photoelectrons ejected from the center of the photocathode produce output pulses whose amplitudes with respect to those produced by photoelectrons ejected from the edge of the photocathode by the same incident particle are greater by 3/2. This effect is attributable to the non-uniform collection efficiency of the photoelectrons by the first dynode, and is dependent on the electrostatic arrangement between the photocathode and first dynode. There is an additional timing error in machine-time since the ejected photoelectrons must travel varying distances to the first dynode of the multiplier structure. Machine time is further influenced by photomultiplier transit time variance due to:

1) Different initial velocities of the photoelectrons, both in angle and magnitude.
2) Different electron paths and different secondary emission electron velocities.
3) Variance in the secondary electron multiplication.

The aforementioned effects combine to vary both the rise times and amplitudes of the fiducial signals at the input to the TPHC. With the type HO cable ($50\Omega = Z_o$) the amplitude spectrum of these fiducial signals ranges from three-fourths to two volts; consequently, the operation of the TPHC ranges between the centroid non-linear and the ballistic linear modes.[30]

Fortunately some of these effects can be calibrated out or accounted for in the fast timing system composed of the detectors and TPHC.

Consider first the Fast Timing System as an electronic black box. With the mercury pulser furnishing parent signals and a fixed time delay between the Start and Stop inputs of the TPHC, the electronic resolution of the Fast Timing System was 1.25 nsec FWHM for the 0-2 side and 1.3 nsec FWHM for the 0-1 side.

However, because the photomultipliers provide signals with an amplitude spectrum, a straightforward measurement of the Fast Timing System resolution with the detectors was not possible. Instead a 0-2 single-sided time-of-flight spectrum of $Pu^{239}$ was obtained by the usual method. Then an accurately calibrated delay line was introduced into the #2 input of the TPHC. As a result, the entire time-of-flight spectrum moved to lower channels of the multichannel analyzer.* Assuming that all of the detector pulses suffer the same attenuation in transmission through the delay line, the number of channels shifted should be the same for each point of the spectrum. This was not the case. The reference spectrum is shown in Figure 17a. Figure 17b shows the spectrum obtained with a 100.9 nsec delay line in line 2-FS of the TPHC. Figure 17c shows the spectrum obtained with a 204.7 nsec delay line introduced in line 2-FS. The digital readout of these photographed spectra were plotted as seen in Figure 19. From these data, it is apparent that the machine-time is dependent on the absolute amplitude of the input signals to the TPHC. Since the effects of signal amplitude and rise time are involved here, the combined effect is called the Amplitude - Rise Time (ART) effect. To establish the validity of the ART effect, consider Figures 17a, b,

---

*ND-130 - 512 Channel Analyzer.

and c. For convenience, these figures have been combined and are represented in Figure 18. The time delay between spectra (a) and (b) was established via a 100.9 nsec delay cable; while the time delay between spectra (b) and (c) was established via an additional 103.8 nsec cable. The assumption is now made that the cable attenuation is independent of the amplitude of the input signals over the amplitude range available. Because the time delays between the spectra are not exactly equal, it was necessary to weight the time per channel for the two cases in order to account for the differential nonlinearity of the TPHC. The following analysis shows how the weighting was performed.

Given a differential linearity curve as shown:

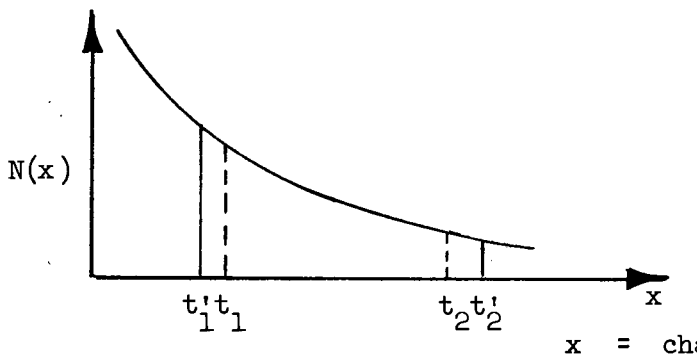


x = channel number

where the primed and unprimed symbols refer to the heavy and light fragment peaks respectively, and subscripts 1 and 2 refer to the delayed and undelayed spectra respectively, then

$$\left.\begin{array}{l}\text{channel \#296} \Longrightarrow t_2' \\ \text{channel \#195} \Longrightarrow t_1'\end{array}\right\} \alpha\bar{T}_H;$$

$$\left.\begin{array}{l}\text{channel \#294} \Longrightarrow t_2 \\ \text{channel \#205} \Longrightarrow t_1\end{array}\right\} \alpha\bar{T}_L.$$

Knowing N(x) versus x as in Figure 19,

$$\bar{T}_H \; \alpha \sum_{x=\#195}^{\#296} N(x) \; \alpha \; t_{195}^{296}; \quad \sum_{x=\#195}^{\#296} N(x) = 31{,}315 \text{ counts}; \tag{15}$$

$$\bar{T}_L \; \alpha \sum_{x=\#205}^{\#294} N(x) \; \alpha \; t_{205}^{294}; \quad \sum_{x=\#205}^{\#294} N(x) = 25{,}635 \text{ counts}. \tag{16}$$

$\bar{T}_H$ = the apparent time measured by the apparatus for a known cable delay; viz., 100.9 nsec, corresponding to fiducial signals produced by the heavy fission fragment. $\bar{T}_L$ = the apparent time measured by the apparatus for an additional known 103.8 nsec (total delay = 204.7 nsec) cable delay corresponding to fiducial signals produced by the light fission fragment.

For no ART effect, the ratios of apparent times to known delay times would be equal; however, for the present cases:

$$\frac{31{,}305 \text{ counts}}{100.9 \text{ nsec}} = 1.22 \text{ counts/nsec} \tag{17}$$

$$\frac{25{,}635 \text{ counts}}{103.8 \text{ nsec}} = 0.972 \text{ counts/nsec} \tag{18}$$

The difference between these two values is 22.8% indicating the importance of the ART effect.

One further analysis of interest can be performed with respect to the ART defect based on the data available in Figure 19. This analysis considers the ART defect formed by the difference in time between the light mass fragment peaks delayed by a known 100.9 nsec, and the time difference between the light and heavy mass fragment peaks of the reference spectrum. The latter time difference is obtained from the data of Milton and Fraser[20] and compared with the present results from these tests; thus:

time difference between delayed light-fragment peaks = 100.9 nsec;

correction due to differential nonlinearity = 3.6%;

time difference between delayed light fragment peaks

$$= 100.9(1 - 0.036) \text{ nsec},$$

$$= 97.27 \text{ nsec};$$

time difference between light and heavy fragment peaks

$$= 96.48 \text{ nsec}.$$

This last figure is obtained from the corrected and best-fit data of Milton and Fraser.[20]

Then (97.27 - 96.48) nsec = 0.79 nsec = time difference between the time intervals corresponding to the light fragment peaks and to the light and heavy fragment peaks of the reference spectrum. This time difference amounts to a timing difference of ~1%.

The conclusion which is drawn from this experiment is that the ART effect is real, especially for the heavy fragment. It may also exist in the reference spectrum but to what extent is not known. Comparison with the data of Milton and Fraser[20] indicates that the performance of this apparatus is comparable with theirs (~1%).

6. Differential Linearity

Generally, the term "differential linearity" arises in describing the characteristic curve of a multichannel analyzer. It is a measure of the uniformity of channel widths over the range of channels available; e.g., a differential linearity of 2% means that no channel departs by more than 2% in width from the average channel width over the entire range of available channels.

With the TPHC, the differential linearity is still a measure of the characteristic curve of the instrument but in the form of a

distribution function of the limit of the width of the time intervals per unit time interval over the entire time range of interest as the time interval goes to zero. It is a much more sensitive evaluation of the instrumental performance than is the integral linearity. Here, the integral linearity may be defined as the ratio of the maximum time departure at any time-point to the true value of that time point expressed as a percentage of full scale time. Obviously, the principal limitation to the use of the integral linearity is the fact that the percentage error of time expressed as the ratio of the actual timing error to the correct time may be huge at small values of time while the integral linearity as defined above may be excellent. In contrast, a differential linearity percentage means that the same percentage error exists over the entire time range of interest.

The differential linearity of a system bears essentially no significance on a measurement provided:

1) it is measurable and known.

2) it remains constant.

Within these two limitations, any differential nonlinearity can be accounted for by proper calibration.

The differential linearity is measured by obtaining a spectrum of random time intervals introduced into the TPHC. Because the time intervals are random and span the time range of interest, an equal number of counts should be stored in each channel of the analyzer if the TPHC characteristic curve is perfectly flat. One difficulty with this measurement lies in the generation of random time intervals. Generally a fixed frequency generator is used to furnish Start pulses to the TPHC

while random Stop pulses are provided by a detector generating signals corresponding to the decay of a radioactive source. Since the radioactive decay is random in time, it is usually tacitly assumed that the time intervals between the regular Start and random Stop signals are random. This is not the case (See Appendix II). It is seen that the time interval distribution is expressed as:

$$P[\geq 1,\ i,\ P(i)] = e^{-r\,T_o}(e^{\bar{n}} - 1), \tag{19}$$

= probability of at least 1 count appearing in a channel weighted with probability P(i),

where: $r$ = random counting rate at Stop input,

$T_o$ = time range of interest,

$\bar{n}$ = average number of counts stored in a channel.

Notice, however, that for $rT_o$ small, the exponential can be expanded in a series:

$$(e^{\bar{n}} - 1)\, e^{-rT_o} = (e^{\bar{n}} - 1)(1 - rT_o + \ldots.), \tag{20}$$

$$= (e^{\bar{n}} - 1)(1) \text{ for } rT_o \ll 1).$$

Thus, for low counting rates and a short time range of interest, the distribution of time intervals is essentially random, i.e., flat.

Figure 20 shows the differential nonlinearity of the 0-2 side of the TPHC (Side 0-1 is basically the same). The time range "$T_o$" and "r" the average counting rate of the random source were:

$T_o$ = 633.95 nsec ,

$r$ = 3000 counts/sec .

From these data, $rT_o = 1.9 \times 10^{-3}$ and the correction to the slope of the distribution of Figure 20 is negligible.

Although the slope of the random time distribution is ~300 counts per channel and in reality violates the criteria of an ideally versatile time analyzer,[33] nevertheless measurements made at widely varying times under the same biasing conditions on the TPHC yielded the same slope within ± 5%. Therefore, for a single-sided spectral run on $Pu^{239}$ lasting 24 hours, the differential linearity can be assumed constant and known.

# CHAPTER IV

## TIME-TO-PULSE-HEIGHT CONVERTER SIGNAL PROCESSING

### A. Signal Characteristics

The shortest fragment-time-of-flight expected is about 180 nsec. The maximum voltage change developed across $C_2$ in the TPHC output follows from Equation (12):

$$\Delta V_c = \frac{I}{C_2} \Delta t. \tag{21}$$

For the case:

(a) $I = 100\ \mu\text{amps}$,

(b) $C_2 = 2200$ pfds,

(c) $\Delta t = (633.8 - 180)$ nsec,

$= 453.8$ nsec,

$$\Delta V_c = \frac{100 \times 10^{-6}}{2200 \times 10^{-12}} \times 453.8 \text{ nsec}, \tag{22}$$

$$= 20.6 \text{ millivolts}.$$

Similarly, the minimum voltage change corresponding to a 500 nsec flight time is:

$$\Delta V_c = 6 \text{ millivolts}. \tag{23}$$

The time constant of the TPHC integrator $RC_2$ is $(2200 \times 10^{-12})(10^5) = 2200 \times 10^{-7}$ sec or 220 μsec. The maximum measured time interval from Equation (21c) is 453.8 nsec; a factor of 1/500 of the integrator time constant; hence, the linearity of the integrator circuit is ensured. Furthermore, the slope of the linear discharge curve is, from Equation (11),

$$\frac{dv}{dt} = \frac{I}{C_2}, \tag{24}$$

$$= \frac{100 \times 10^{-6}}{2200 \times 10^{-12}} = 45 \times 10^{3} \text{ amps/fd.}$$

Summarizing, the output signal from the TPHC has these properties:

1) Voltage range: $6 \text{ mv} \leq \Delta V_c \leq 21 \text{ mv}$,

2) Slope: $45 \times 10^3$ amps/fd and linear,

3) Time constant: 220 μsec.

This output signal is fed into a preamplifier shown schematically in Figure 5. The input time constant of the preamplifier is:

$$RC = (100 \times 10^{6})(1000 \times 10^{-12}), \tag{25}$$

$$= 10{,}000 \ \mu\text{sec}.$$

Thus, the preamplifier input circuit is an integrator and follows the TPHC output signal closely. The rest of the preamplifier is of conventional design except for incorporating a White cathode follower output stage. This design feature was introduced to drive lengths of 100 feet of RG62/U coaxial cables so that much of the apparatus could be operated at remote locations.

The preamplifier gain is nominally 15; thus the signal amplitude available at the preamplifier output ranges from 90 mv to 215 mv.

This signal is in turn fed into a standard A-1 amplifier set at a 0.5 Mc bandwidth. It is in the A-1 amplifier that the signal is differentiated and pulse shaped. Because the input signals are differentiated, the disparity in the time constants between the TPHC output and preamplifier input does not lead to any D.C. level shifts due to pulse pileup for count rates up to 1000 counts/sec. The output signals of the

A-1 amplifiers were set by the gain adjustment to range between 25 volts and 85 volts. Outside this range, slight nonlinearities basic to the A-1 amplifier manifest themselves.

## B. Drift and Gain Stability

Several tests were run to establish the gain stability and drift figures of the Fast Timing Systems consisting of the TPHC, preamplifier, A-1 amplifier and multichannel analyzer.* Two sets of tests were performed each employing an ORNL Q-1212 mercury pulser furnishing pulses which with suitable delay cables formed two fixed time intervals; viz., a 100.9 nsec interval and a 204.7 nsec interval. The first test consisted of noting the channel number in which the fixed time intervals were initially registered and checking each hour whether or not the channel numbers changed. Over a normal twelve hour working day, no single hour check revealed a shift of more than one half channel in either channel number. Although it is extremely difficult to discern whether the shifts were due to gain or bias changes, the fact that the shifts were small indicated that they could be balanced by a gain change in the A-1 amplifier. Indeed this was the case.

The second test consisted of an uninterrupted sixteen hour run with the same setup as in the first test. This test was accompanied by a four Farenheit degree temperature change and showed a four channel shift, equivalent to about a 5 nsec change.

---

*Nuclear Data Corporation, 512 channel analyzer model ND130.

From these tests it was concluded that a run could be reasonably free of drifts if the apparatus were checked at least once every two hours with the pulser technique. Note, however, that this method simply checks the drifts in the Fast Timing System exclusive of the detectors. It should be noted further that it is not only the detector signal amplitude and rise time which were responsible for the TPHC response but also the detector signal-to-background ratio as well as the absolute value of the signal and background. The fact that statistically significant, and legitimate spectra can be obtained with this apparatus is due to the high level of reproducibility inherent in it for operating times consonant with sufficiently long counting times.

# CHAPTER V

## SLOW CHANNEL

### A. Signal Characteristics

The slow or coincidence channel consists of the signals derived from the tenth dynodes of all three detectors. These signals are characterized by somewhat longer rise times (~5 nsec) and smaller but positive amplitudes. Deriving these signals from the tenth dynodes of the detectors providing the timing signals yields a measure of validity to both signals. The tenth dynode or "slow" signals are amplified by a preamplifier-amplifier chain identical to the one described under Signal Processing; however, the output signal from the final A-1 amplifier is processed differently.

### B. Coincidence Constraints and Characteristics

Instead of using the normal pulse-shaped output of the A-1 amplifier, the PHS (Pulse Height Selected) output (a discriminator circuit) is used to trigger a double coincidence circuit for single sided spectra or a triple coincidence circuit for correlated spectra. However, the normal PHS output signal is a 25 volts negative pulse, one-half μsec wide at its base and is obtained by differentiating a signal directly proportional to the main signal of the amplifier. Since the coincidence circuit requires a signal about 15 volts negative, the normal PHS pulse at 15 volts amplitude is only 325 nsec wide. With flight times ranging from 180 to 500 nsec, it is obvious that many true coincidences corresponding to the

flight times of the heavy fragments will be lost and the resultant spectrum biased in favor of the lighter, faster fragments. To this end, the circuit shown schematically in Figure 6 was devised. It is a single shot univibrator which produces fixed amplitude (20 volts) negative pulses of adjustable time duration. The time duration is controlled by the variable 7-45 pfd capacitor. Figure 7 shows the optimum pulse durations employed in establishing the coincidence constraint. The A-1 output pulses reach their maximum amplitude in one and one-half μsec; as a consequence, a time delay is introduced into the coincidence constraint. The PHS potentiometer is used to discriminate against illegitimate pulses which contribute to the accidental coincidence counting rate; however, at a given PHS bias setting, an A-1 pulse must have an amplitude sufficient to overcome this bias. With a one and one-half μsec time-rise response, an A-1 pulse is delayed for a specific portion of this time rise before the PHS output circuit can be tripped. Figure 7 was drawn with the condition that both A-1 amplifiers associated with the remote detectors were set at the usual setting of 500/1000 units with fixed gains. This setting corresponds to a time delay of about one μsec before the univibrator could be tripped. Furthermore Figure 7 corresponds to the situation for the slowest and fastest fragment flight times. Since all constraints are satisfied for this limit, it follows that the constraints are satisfied for all intermediate cases. It is this time delay which accounts for the use of external one μsec delay lines at the output of the A-1 amplifiers of the Fast Timing Systems. Without them, the signals to be analyzed would appear at the input to the analyzer before the coincidence

constraint was satisfied; thus, the analyzer would record erroneous signals or none at all.

The multichannel analyzer used for recording, storing, and displaying the spectra of the fission fragments' time-of-flight is the ND130.* It has 512 channels with choice of 127, 255, or 511 point analysis; its integral linearity is rated at better than 0.5% of full scale while its differential linearity is typically better than 1% over 98% of its range. The zero drift of the analyzer is listed at less than 0.5% of full scale per 24 hours, and less than 0.5% of full scale per $10^{\circ}$F. A typical drift figure is ± 0.1% per day. Similarly, the gain drift is listed at less than 1% of full scale per 24 hours and less than 1% of full scale per $10^{\circ}$F.

---

*Purchased from Nuclear Data, Inc.

# CHAPTER VI

## ANALYSIS OF THE EXPERIMENTAL TIME MEASUREMENT

### A. Detector Transit Times

The details of the various transit times encountered in measuring the flight times of fission fragments are developed in this section. Consider Figure 20. This is a diagram of the zero detector with its salient features and dimensions labelled.

Consider first the transit time of a single secondary electron from the 3 μin. Ni foil, (Ni) to the scintillator (Si). For simplicity, consider the electron ejected from the very center of (Ni). (It should be noted in passing that the term secondary electron is preferred to delta rays, because delta rays are defined[32,33] as electrons ejected with energies greater than 1000 ev, whereas secondary electrons have energies limited to, at most, a few hundred ev.) Assuming that the electron speed never exceeds a small fraction of the speed of light, it follows from the conservation of energy that:

$$\frac{1}{2} m_e v_2^2 - \frac{1}{2} m_e v_1^2 = q(V_2 - V_1). \tag{26}$$

For secondary electrons $v_1$ is negligible, and for the case in Figure 20, $V_1 = 0$ volts; hence

$$\frac{1}{2} m_e v_2^2 = q\, V_2. \tag{27}$$

For the purposes of estimating the transit time of the secondary electrons from the nickel foil (Ni) to the scintillator (Si), consider the secondary electrons to travel on the center line between (Ni) and (Si) and

that the electric field is uniform along this center line. For this case Newton's Second Law of Motion yields:

$$|\vec{F}| = \frac{d^2S}{dt^2} m_e . \tag{28}$$

$$|\vec{E}| = \frac{|\vec{F}|}{q} = \frac{V_2}{d} . \tag{29}$$

$$\therefore \quad \frac{V_2 q}{d} = m_e \frac{d^2S}{dt^2} , \tag{30}$$

or

$$\frac{d^2S}{dt^2} = \frac{V_2 q}{m_e d} . \tag{31}$$

Integrating Equation (31) under the boundary conditions that $\frac{dS}{dt} = 0$ at $t_e = 0$ yields

$$\frac{dS}{dt} = v = \frac{V_2 q}{m_e d} t_e . \tag{32}$$

Here, "v" is the speed of the electron evaluated at a point on its straight line path at time "$t_e$."

A second integration yields, under the same boundary conditions:

$$S = \frac{V_2 q}{2 m_e d} t_e^2 . \tag{33}$$

Solving Equation (33) for "$t_e$" at S = d yields the electron transit time from Ni to S

$$t_e = \left[\frac{2d^2 m_e}{qV_2}\right]^{1/2} . \tag{34}$$

For: $d = 6.67$ cms,

$m_e = 9.1 \times 10^{-28}$ gms,

$$qV_2 = (1.6 \times 10^{-12} \text{ ergs/ev})(15 \times 10^3 \text{ ev}).$$

Equation (22) yields,

$$t_e = 1.8 \text{ nsec.} \tag{35}$$

Since the field is considered uniform, $t_e = 1.8$ nsec would equal the transit time for secondary electrons anywhere on the foil; however, this assumption is too restrictive. Actually a field plot of the lens shows some non-uniformity, and this naturally leads to a spread in transit time. Fraser and Milton,[34] and Stein and Leachman[22] using basically the same lens structure measured transit time spreads of 2.5 to 5 nsec FWHM. This time spreads includes all instrumental effects, the largest of which are those inherent in the photomultiplier. Following Gatti,[25] the variance in the timing signal due to photomultiplier transit time spread for this apparatus amounts to 1.2 nsec$^2$. A reasonable assumption based on the electrostatic lens field plot is that the variance in electron transit time spread between Ni foil and scintillator is no greater than 0.2 nsec$^2$. Since the electron transit time variance and the photomultiplier transit time variance are stochastically independent, the overall variance of the zero time fiducial signal is

$$\sigma^2_{0-T} = \sigma^2_{t_e} + \sigma^2_{PMT}, \tag{36}$$

$$= (0.2 + 1.2) \text{ nsec}^2.$$

With the further assumption that these transit time spreads are normally distributed, the FWHM, W, is:

$$W_{0-T} = 2.35\, \sigma_{0-T}, \tag{37}$$

$$= 2.35 \times 1.2 \text{ nsec},$$

$$= 2.8 \text{ nsec}.$$

## B. Velocity Expressions

Figure 21 shows the salient parameters labelled for determining the time relationships of the correlated flight times of the fission fragments. This development is necessary because the zero-of-time detector is asymmetrically located in the flight path of the fragment pair and the velocity loss of the fragments through the various nickel foils is a function of fragment mass and velocity.

Case I: Fissile source deposit directed toward 0-2 flight path.

Let: $t_2$ = fragment flight time from secondary electron Ni foil to detector #2,

$t_e$ = electron flight time from secondary electron Ni foil to the zero detector,

$T_o$ = zero cable delay time,

$t_{SF_2}$ = fragment flight time from fissile source to secondary electron Ni foil,

$v_2$ = velocity of the 0-2 fission fragment after it passes through the secondary electron Ni foil.

By definition,

$$v_2 = \frac{d_{FD_2}}{t_2} . \tag{38}$$

In traversing the Ni foil, the fragment loses a fraction of its velocity; call this fraction $\rho(v,m)$ since the energy loss depends on the fragment mass and entrant velocity.

Then, the time-of-flight of fragment 0-2 from the Ni foil to detector #2 is:

$$t_2 = t_2' + t_e, \tag{39}$$

where: $t_2'$ = "measured" flight time between the arrival of signals at detector #2 and the zero detector.

However, the flight time $t_2'$ is <u>not</u> what is measured in the experiment. It is $t_2''$, which is the supplement of the flight time.

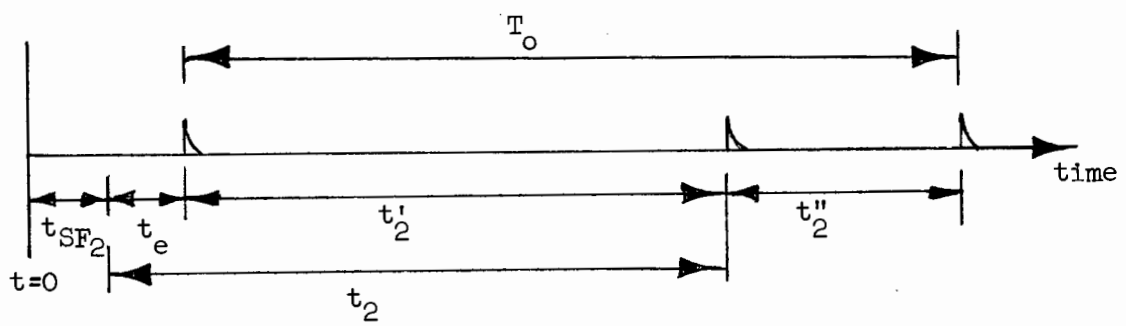


Time Sequence for Cases I and II

$$\therefore \quad t_2'' = T_o - t_2'. \tag{40}$$

Combining Equations (39) and (40) yields

$$t_2 = T_o - t_2'' + t_e. \tag{41}$$

Therefore,

$$v_2 = \frac{d_{FD_2}}{(T_o - t_2'' + t_e)}. \tag{42}$$

Leachman and Schmitt[35] have measured the velocity loss of fission fragments through Ni foils and have found that the heavy and light fragments suffer different attenuations depending on the fragment mass and initial velocity. For the present, a functional relationship can be written for the velocity loss in the form:

$$\rho(v_{SF_2}, m_{0-2}) = \frac{v_2}{v_{SF_2}} = \rho. \tag{43}$$

Hence:

$$v_{SF_2} = \frac{1}{\rho} \frac{d_{FD_2}}{(T_o + t_e - t''_2)}, \tag{44}$$

= post-neutron emission velocity of the 0-2 fragment.

The assumption has been made that the fissile source is so oriented that the 0-2 fission fragment traverses only the secondary electron Ni foil. For the case where the fissile source is directed toward the 0-1 flight path, the 0-2 fission fragment must penetrate the source backing which is also a Ni foil assumed identical to the secondary electron Ni foil.

Case II: Fissile source deposit directed toward 0-1 flight path.

Assume that the 0-2 fragment starts with the same velocity it had in the first case.

$$\therefore \quad v'_{SF_2} = v_{SF_2},$$

where the prime refers to the present case.

Then,

$$v'_{SF_2} = \frac{v''_{SF_2}}{\rho},$$

where $v''_{SF_2}$ is the fragment velocity between the Ni foils, and $\rho$ is defined analogously to Equation (43).

Let: $v'_2$ = velocity of the 0-2 fragment after it traverses the secondary electron Ni foil.

$$v'_2 = \frac{d_{FD_2}}{(T_o - t''_{2_B} + t'_e)}. \tag{45}$$

Here $t'_e$ = electron transit time corresponding to a lower velocity fragment which, because the electron emergence velocity is assumed negligible, is equal to $t_e$.

Now $\quad v''_{SF_2} = \frac{v'_2}{\rho'}$ following Equation (43).

Hence,

$$v_{SF_2} = \frac{1}{\rho'\rho} \frac{d_{FD_2}}{(T_o + t'_e - t''_{2B})}. \tag{46}$$

Note that $t''_2 \neq t''_{2_B}$; in fact $t''_2$ is actually greater than $t''_{2_B}$ based on physical reasoning. About all that can be safely stated about Equations (42) and (45) is that $v_2 \neq v'_2$; experimentally, however, much information, in principle, is deducible from reorienting the source deposit. By obtaining single sided time-of-flight spectra with the fissile source directed first in one direction then the other and comparing the two results, the shift between the spectra will be a measure of the fragment velocity loss through Ni foil; it is evident, therefore, that the calibration for fragment velocity loss through the foils is inherent in the apparatus.

Case III: Fissile source deposit directed toward 0-1 flight path.

Case I showed the analytical development for the 0-2 fragment. The present case will treat the 0-1 fragment.

$$v_1 = \frac{d_{SD_1}}{t_1}, \tag{47}$$

where: $v_1$ = post-neutron emission velocity of the 0-1 fragment;

$t_1$ = fragment flight time from source to detector #1;

$d_{SD_1}$ = distance from source to detector #1.

But,

$$t_1' = t_1 - (t'_{SF_2} + t_e), \tag{48}$$

= flight time between arrival of signals between detector #1 and the zero detector;

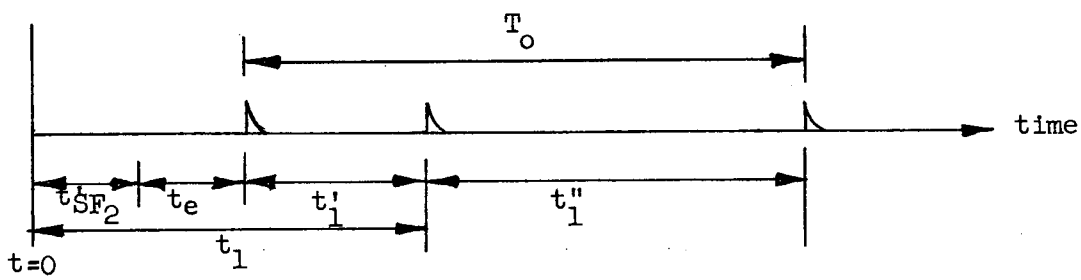


Time Sequence for Cases III and IV

$t_1''$ = measured supplement of 0-1 fragment measured flight time;

$$t_1' = T_o - t_1''. \tag{49}$$

Hence:

$$t_1 = (T_o - t_1'') + t'_{SF_2} + t_e. \tag{50}$$

Here $t'_{SF_2}$ = flight time of the 0-2 fragment traversing the source backing and secondary electron Ni foils,

$$= \frac{d_{SF_2}}{d_{FD_2}} (T_o + t_e - t_2''). \tag{51}$$

Combining these results yields:

$$v_1 = \frac{d_{SD_1}}{(T_o + t_e - t_1'') + \frac{d_{SF_2}}{d_{FD_2}}(T_o + t_e - t_2'')} . \tag{52}$$

Note that $v_1$ is correlated with $v_2$.

Case IV: Fissile source deposit directed toward 0-2 flight path.

Following Equation (47),

$$v_1' = \frac{d_{SD_1}}{t_1'} . \tag{53}$$

The 0-1 fragment will suffer a velocity loss in traversing the Ni source backing; this velocity loss will require that the fragment flight time change.

$$t_1' = (T_o - t_{1_B}'') + t_{SF_2} + t_e . \tag{54}$$

$t_{SF_2}$ = flight time of the 0-2 fragment traversing only the secondary electron Ni foil.

The time $t_{1_B}''$ is different from $t_1''$ since the 0-1 fragment traverses the source backing, $t_{1_B}''$ being in fact a shorter time interval than $t_1''$. Hence:

$$v_1' = \frac{d_{SD_1}}{(T_o + t_e - t_{1_B}'') + \rho \frac{d_{SF_2}}{v_2}} , \tag{55}$$

where: $v_2 = \frac{d_{FD_2}}{(T_o + t_e - t_2'')} .$

Note here again that $v_1'$ is correlated with $v_2$.

In each of the four cases, only one variable is recorded; viz., t". The term $\rho$ containing the velocity loss information can in principle be programmed into a computer. Reference to the work of Schmitt and Leachman[35] and Fulmer[36] indicates that the median light-fragment velocity loss and the median heavy-fragment velocity loss through three microinch thick Ni foils are:

$$(\Delta v_2)_L = 0.27 \times 10^8 \text{ cm/sec}, \tag{56}$$

$$(\Delta v_2)_H = 0.25 \times 10^8 \text{ cm/sec}. \tag{57}$$

C. The Effects of Prompt Neutron Emission

The conservation equations used in the Introduction do not account for the effects of prompt neutron emission on the flights of the fission fragments except insofar as the average fragment velocity is approximately equal to the fragment initial velocity based on the assumption of isotropic neutron emission in the center-of-mass coordinate system of the moving fragment. Actually, the conservation equations apply prior to neutron emission, for in a time of the order of $10^{-14}$ sec of the scission, all the prompt neutrons are emitted.[37] The distance transversed by a fragment in this time is equivalent to $10^7$ nuclear diameters of $Pu^{239}$. The fundamental assumption of isotropic emission of neutrons in the center-of-mass coordinate system of the moving fragment is made on the basis that the measured angular distribution of emitted neutrons is consistent with this assumption.[21]

The effects of prompt neutron emission of the flights of fission fragments are:

1) Data prejudice due to recoil of the fragments as a result of neutron "boil-off."

2) A variance in velocity of the fragments.

The first effect is minimized by a choice of proper geometry. In the present apparatus, all three detectors are the same size except that the #2 detector can scan a distance corresponding to three detector diameters. Specifically, each 6810-A photomultiplier is nominally two inches in diameter; therefore, detector #2 has been designed to scan a six inch distance perpendicular to the 0-2 flight path. In this way, fission-fragment coincidence losses are minimized and the data properly weighted against those cases where the fewest prompt neutrons are emitted. In a detailed calculation by Lide,[38] it is shown for such an arrangement that a proper representation of better than 96% of all the fragments reaching the #1 detector will be intercepted by the #2 detector along its allowable scanning distance.

The second effect introduces a variance in the pre-prompt neutron emission velocities of the fragments. Prompt neutron emission at all directions will administer a component of velocity change to the fragment in the form of recoil. Therefore, although it is still true that the average fragment velocity is equal to the fragment initial velocity, a correction should be supplied to the fragment velocities as given by Equations (44), (46), (52), and (55) to account for the effects of the prompt neutron emission. A detailed formulation of this correction requires determinations of number, energies, and direction of emission of the prompt neutrons. Since such information is not obtained in this experiment, the change in velocity due to neutron emission from the

fragments is treated as a variance in the time-of-flight data; this then is reflected as an additional variance in velocity, mass (as deduced from momentum and mass conservation), energies, etc.

Lide's[38] detailed calculation for the effects of prompt neutron emission on the time of flight of fission fragments is summarized below. Assuming a Watt distribution for the energy of neutrons emitted as a function of mass, Lide showed that the variance in time of arrival for a fragment emitting k neutrons and having a flight time $t_o$ when no prompt neutrons are emitted is given by:

$$\sigma^2(t_k - t_o) = k\,\varkappa_k \frac{t_o^2}{4}, \tag{58}$$

where:

$$\varkappa_k = 2mT\left[\frac{M}{(M - km)P_i}\right]^2, \tag{59}$$

$m$ = neutron mass,

$T$ = nuclear "temperature," a parameter used in fitting neutron spectra with the Watt neutron-energy formula,

$P_i$ = initial momentum of the fission fragment,

$M$ = mass of the fission fragment before neutron emission.

For this experimental arrangement, using $Pu^{239}$ as the fissile source, the timing variances introduced by prompt neutron emission are:

$$\begin{aligned} \sigma^2_{0\text{-}2_H} &= 8.024\ \text{nsec}^2, \\ \sigma^2_{0\text{-}2_L} &= 4.20\ \text{nsec}^2, \\ \sigma^2_{0\text{-}1_H} &= 6.161\ \text{nsec}^2, \end{aligned} \tag{60}$$

$$\sigma^2_{0\text{-}1_L} = 3.22 \text{ nsec}^2,$$

where: $\sigma^2$ = variance,

H = heavy fragment,

L = light fragment,

0-1 and 0-2 = flight paths.

# CHAPTER VII

## PRECISION OF THE EXPERIMENT

### A. Precision Indices of the Apparatus

The largest variance in timing-signal spread from each of the three detectors is due to the transit time spread of the photomultiplier tubes. Following Gatti[25] and the experimental work of Bartl and Weinzierl,[43] this variance amounts to about 1.2 $nsec^2$.

The variance in the measurement of the delay cable is negligible (See Table I).

The variance in zero-detector secondary electron transit time is 0.2 $nsec^2$ [See Equation (36)].

The flight paths have been measured to ± 0.08 cm. Since each flight path is greater than 300 cm, the error of the distance measurement is less than 0.02% and is negligible when compared with the error due to photomultiplier transit time spreads.

### B. Precision Index Due to Effects of Prompt Neutron Emission

Lide's[38] calculations show that the variances in $Pu^{239}$ median fission fragment average transit time over the flight paths of this experiment are:

$$\sigma^2_{0-2_H} = 8.024 \text{ nsec}^2,$$

$$\sigma^2_{0-2_L} = 4.20 \text{ nsec}^2,$$

$$\sigma^2_{0-1_H} = 6.161 \text{ nsec}^2,$$

$$\sigma^2_{0\text{-}1_L} = 3.22 \text{ nsec}^2 .$$

C. Corrections

The velocity loss due to the $Pu^{239}$ fission fragment traversing the nickel foils amounts to a maximum of 2.5% for the median-heavy fragment; however, the fragment velocity loss in traversing a nickel foil is a function of the fragment mass and velocity. Schmitt and Leachman[35] show that the velocity loss near the beginning of the range can be expressed by a somewhat arbitrary expression,

$$\frac{dv}{dx} = - Av^n ,$$

where A and n are considered to be functions of only the fragment mass, the velocity v is in $(10^8)$ cm/sec, and the foil thickness x is in $mg/cm^2$. To account for this velocity loss on a per fission basis would require a computer program to make the required corrections in the velocities as described by Equations (51) and (66) or (57) and (63) depending on the fissile source orientation. Short of this computer procedure, the 2.5% velocity loss will be used in estimating the overall precision in the velocity measurement. This means that $\rho_{max}$ defined in Equatio (46) will be 0.975.

It shall be assumed that the ART effect can be accounted for by calibration and will be ignored in the precision evaluation.

D. Best Estimate of Precision of the Velocity Measurements

Case I: Fissile source toward 0-2 flight path from Equation (51).

$$v_{SF_2} = \frac{1}{\rho} \frac{d_{FD_2}}{(T_o + t_e - t_2'')}.$$

Hence,

$$\sigma^2_{v_{SF_2}} = \frac{1}{\rho^2} \frac{d^2_{FD_2} \sigma^2_t}{(T_o + t_e - t_2'')^4}, \tag{61}$$

= variance in the post neutron emission velocity of the 0-2 fragment.

$\sigma^2_t$ = variance in timing including the effects of prompt neutron emission.

The expression for $\sigma^2_{v_{SF_2}}$ is now evaluated with the following quantities:

$$(T_o + t_e - t_2'') = 247.01 \text{ nsec},$$

$$\sigma^2_t = (1.2 + 0.2 + 4.2 + 1.2) \text{ nsec}^2,$$

or

$$\sigma^2_t = 6.8 \text{ nsec}^2,$$

$$d_{SF} = 14.0 \text{ cms},$$

$$d_{FD_2} = 329.84 \text{ cms},$$

$$\rho = 0.975.$$

From these data,

$$\sigma^2_{v_{SF_2}} = \frac{d^2_{FD_2}}{\rho^2} \frac{\sigma^2_t}{(T_o + t_e - t_2'')^4}, \tag{62}$$

$$= \frac{1.09 \times 10^5}{0.95} \left(\frac{6.8 \times 10^{-18}\ \text{sec}^2}{37.2 \times 10^{-28}\ \text{sec}^4}\right),$$

$$= (2.1)10^{14}\ \text{cm}^2/\text{sec}^2.$$

The standard deviation, $\sigma_{v_{SF_2}}$, becomes,

$$\sigma_{v_{SF_2}} = 1.4 \times 10^7\ \text{cm/sec.} \tag{63}$$

For the FWHM for a Gaussian distribution yields:

$$\text{FWHM}_{v_{SF_2}} = 2.35\ \sigma_{v_{SF_2}}, \tag{64}$$

$$= 3.4 \times 10^7\ \text{cm/sec.}$$

Case II. Fissile source toward O-1 flight path

$$v_{SF_2} = \frac{1}{\rho\rho'} \frac{d_{FD_2}}{(T_o + t'_e - t''_{2B})}. \tag{65}$$

For simplicity, assume $\rho = \rho'$; then,

$$v_{SF_2} = \frac{1}{\rho^2} \frac{d_{FD_2}}{(T_o + t'_e - t''_{2B})}.$$

$$\sigma^2_{v_{SF_2}} = \frac{1}{\rho^4} \frac{d^2_{FD_2}}{(T_o + t'_e - t''_{2B})^4} \sigma^2_t, \tag{66}$$

$$= 1.1 \left(\frac{1.09 \times 10^5}{39.9 \times 10^{-36}}\right)(6.8 \times 10^{-18}),$$

$$= 2.2 \times 10^{14}\ \text{cm}^2/\text{sec}^2.$$

The standard deviation becomes:

$$\sigma_{v_{SF_2}} = 1.48 \times 10^7\ \text{cm/sec}, \tag{67}$$

$$\text{and the FWHM} = 1.48 \times 10^7 \times 2.35, \tag{68}$$
$$= 3.48 \times 10^7 \text{ cm/sec.}$$

Because the precision indices of the 0-1 flight side are the same, the following summary can be made: viz, the "best value" estimate of a single sided velocity measurement can be made with a precision of $2 \times 10^7$ cm/sec.

The variance in the mass as defined by Equation (4) can also be determined since it depends only on the correlated velocities.

From Equation (4),

$$M_1^* = \frac{A+1}{1+\frac{v_1}{v_2}}; \quad \frac{\partial M_1^*}{\partial v_1} = \frac{-(A+1)v_2}{(v_1+v_2)^2}; \quad \frac{\partial M_1^*}{\partial v_2} = \frac{-(A+1)v_1}{(v_1+v_2)^2}.$$

From which,

$$\sigma^2_{M_1^*} = \frac{(A+1)^2}{(v_1+v_2)^4}\left(v_1^2\,\sigma^2_{v_1} + v_2^2\,\sigma^2_{v_2}\right). \tag{69}$$

For $Pu^{239}$,

$$\bar{v}_L = 1.39 \times 10^9 \text{ cm/sec},$$
$$\bar{v}_H = 1.001 \times 10^9 \text{ cm/sec},$$
$$\bar{\sigma}^2_{v_{2_L}} \leq 4 \times 10^{14} \text{ cm}^2/\text{sec}^2,$$
$$\bar{\sigma}^2_{v_{1_H}} \leq 4 \times 10^{14} \text{ cm}^2/\text{sec}^2.$$

Evaluating Equation (69) with these values yields:

$$\sigma^2_{M_1^*} = 2.07 \text{ amu}^2. \tag{70}$$

$$\therefore \quad \sigma_{M_1^*} \leq 2 \text{ amu}.$$

Note that this value for the mass variance was obtained for the average velocities of the fission-fragment masses at the peaks of the mass distribution spectrum for $Pu^{239}$.

Even though it has been assumed that the ART effect can be accounted for by calibration, it is instructive to evaluate the fission fragment mass variance by taking into account the ART effect as a systematic error. It has been shown that the ART effect varies from as little as 1% to more than 10% in measured time. Consider the case where the ART effect is equal to 10%. This means that the heavy fragment flight time will be 10% less than it should be. The light fragment velocity will be assumed unchanged. Then:

$$\bar{v}_L = 1.39 \times 10^9 \text{ cm/sec},$$
$$\bar{v}_H = 1.001 \times 10^9 \text{ cm/sec} \Longrightarrow 0.91 \times 10^9 \text{ cm/sec},$$
$$\sigma^2_{L,H} = 4 \times 10^{14} \text{ cm}^2/\text{sec}^2 .$$

Evaluating Equation (60) with these new values yields:

$$\sigma^2_{M^*_1} = 2.27 \text{ amu}^2. \tag{71}$$

Neglecting the ART effect, $\sigma^2_{M^*}$ was equal to 2.07 $\text{amu}^2$. Comparing the two results shows that a 10% ART effect in the peaks of the velocity distribution corresponds to an increase of ~10% in the mass variance and an increase in calculated mass of ~5%.

# CHAPTER VIII

# CONCLUSIONS

## A. Detector Improvements

The spectrum of the flight time of the fission fragments obtained by each side of the double time-of-flight apparatus highlights the fact that once the apparatus is properly tuned, the data are highly reproducible. Based on this fact, the apparatus must be considered an effective research tool.

It has been demonstrated that signal-to-background ratios in the detectors, amplitude-rise time effects in the TPHC, and limitations of calibration techniques are the basic limitations of this apparatus. Consequently, a number of steps can be taken which should improve the operation of the apparatus.

Consider the problem of signal-to-background ratios in the detectors. The zero detector has always been characterized by a great deal of noise. Investigations of the quartz light pipes disclosed that manganese impurities in the quartz produced scintillations under gamma ray bombardment. The quartz was initially cooled to liquid nitrogen temperature and exposed to $Co^{60}$ gamma rays. After an eight hour exposure at $3.39 \times 10^4$ R/min, the quartz was removed from the liquid nitrogen and allowed to warm to room temperature in a darkened room. As a consequence of the warming, trapped excited states in the quartz decayed to their ground states. The light accompanying the decay was in the visible blue region. It is in this region that the photocathode response is

maximum (S-11 response for a 6810-A photomultiplier). Furthermore, when the quartz was examined spectrophotometrically and compared with an un-irradiated quartz sample from the same stock, the irradiated quartz showed a change in optical density of 0.04 which corresponds to an absorption increase of 10%. This increase in opacity can account for the increase of einzel lens voltage necessary to reproduce the same signal output from the zero detector while the apparatus was being operated for the last two years. The first problem can be solved by resorting to non-scintillating, non-discoloring ultra-pure quartz, which can now be purchased commercially.

A second, more insidious problem concerns the emission of Compton secondary electrons from the einzel lens structure by the gamma rays emanating from the reactor. Gamma ray energies ranging between 0.2 and 2 mev can generate Compton secondary electrons ranging from 10 kev to 1000 kev, which is the same energy range for secondary electrons ejected from the Ni foils by the fission fragments and accelerated by the lens. This background was minimized by making the neutron beam hole approximately equal in size to the fissile deposit.

A third consideration involving signal-to-background ratios in detectors revolves about electronic component selection; e.g., the oil-filled coupling capacitors of the photomultiplier tubes should be replaced by dry dielectric capacitors for improved dependability of service. Such high voltage rated capacitors are now commercially available and are physically small so that inductive-capacitive effects of the device do not influence the photomultiplier output pulse rise time.

Bellettini, et al,[39] have recently studied the effects of varying independently the inter-dynode voltages of photomultiplier tubes. They found that great improvements are possible over the performances obtainable with the voltage distributions recommended by the manufacturers; i.e., peak currents, linearity and photocathode inefficiency effects can be improved and that timing resolutions better than 1 nsec are possible. However, each photomultiplier tube of a given type had its own voltage characteristics so that generalizations about optimum voltages were not possible. Obviously, such a procedure would be employed only after all other sources of timing dispersion were reduced to a value below those introduced by the photomultiplier tubes.

## B. Circuit Improvements and Criteria

No matter what is done to improve the signal-to-background ratio of the detectors, there remains the problem of pulse amplitude spectrum due to photocathode inefficiency, and the associated "walks" and "jitters" in the resulting signals. It is imperative that the pulses from the photomultipliers be shaped in a standard way before they are made to trigger a TPHC. No matter what device is used for pulse standardization, the same limitations of the photomultiplier signals in triggering circuits are manifested in such devices also, albeit reduced in import.

Insertion of any device, be it an amplifier or a tunnel-diode discriminator,[40] between detector and TPHC cannot improve timing information below the basic limitations inherent in producing fiducial timing signals produced by scintillator-photomultiplier tube combinations.[30] Therefore, it appears logical that improvements in resolution of these

are in order. Sternglass and Wachtel[41] report on a novel approach to multiplier action. They employ transmission-emission multiplication rather than secondary emission multiplication as is now conventionally done. In this approach, the transmission multiplier plates are curved and stacked as a parallel structure, and the individual plates raised to various voltages as is done with secondary emission multipliers. To improve the resolution and reduce pulse widths and transit time spreads, the entire assembly is placed in a magnetic shield. It is the combination of the electric fields and magnetic shielding which produces the improvements. The focusing action tends to reduce transit time spreads, to produce more uniform pulses than do conventional multipliers, and to improve fiducial timing information. As yet, such detectors are not commercially available.

An improvement in signal-to-background ratios in the detectors should, of course, be tempered by the knowledge that not only should signal size be increased but also that the background should be reduced. The reason for this becomes clear when one considers the premise behind fast-slow coincident techniques. In essence, only those events are acceptable for analysis which satisfy the slow coincidence constraint. It is normally assumed that unwanted or meaningless events are ignored. This is not the case, for at high counting rates composed of any ratio of acceptable to ignorable events, D.C. base line shifts can occur. The A-1 amplifiers used with this time-of-flight apparatus are characterized by D.C. level shifts amounting to one channel of the ND130 multichannel analyzer at counting rates of about 1000 counts/sec.

# BIBLIOGRAPHY


1. Marion, J.B., and J.L. Fowler, Fast Neutron Physics, Interscience Publishers, Inc., New York, 1960.

2. Sharpe, J., Nuclear Radiation Detectors, John Wiley & Sons, Inc., New York, 1955.

3. Chase, R.L., Nuclear Pulse Spectrometry, McGraw-Hill Book Co., Inc., New York, 1961.

4. Worthing, A.G., and J. Geffner, Treatment of Experimental Data, John Wiley & Sons, Inc., New York, 1947.

5. Blatt, J.M., and V.F. Weisskopf, Theoretical Nuclear Physics, John Wiley & Sons, Inc., New York, 1954.

6. Klemperer, O., Electron Optics, University Press, Cambridge, 1939.

7. Present, R.D., Kinetic Theory of Gases, McGraw-Hill Book Co., Inc., New York, 1958.

8. Bradley, J.E.S., Physics of Nuclear Fission, Pergamon Press, New York, 1958.

9. Petit, J.M., Electronic Switching, Timing, and Pulse Circuits, McGraw-Hill Book Co., Inc., New York, 1959.

10. Slater, J.C., Microwave Transmission, McGraw-Hill Book Co., Inc., New York, 1942.

11. Gillespie, A.B., Signal, Noise and Resolution in Nuclear Counter Amplifiers, McGraw-Hill Book Co., Inc., New York, 1953.

12. Martin, L., Advances in Electronics II, Academic Press, Inc., New York, 1950.

13. Evans, R.D., The Atomic Nucleus, McGraw-Hill Book Co., Inc., New York, 1955.

14. Fairstein, E., Pulse Amplifier Manual, ORNL-3348, 1962.

15. Bewley, L.V., Two-Dimensional Fields in Electrical Engineering, The MacMillan Co., New York, 1948.

16. Bell, D.A., Electrical Noise, D. Van Nostrand Co., Ltd., London, 1960.

17. Hyde, E.K., A Review of Nuclear Fission, UCRL-9036, 1960.

18. Dynkin, E.B., Theory of Markov Processes, Pergamon Press, London, 1960.

## REFERENCES


1. O. Hahn and F. Strassman, Naturwiss 27, 11 (1939).
2. O. Hahn and F. Strassman, Naturwiss 27, 89 (1939).
3. L.E. Glendenin, et al, Phys. Rev. 84, 860 (1951).
4. H.G. Thode and R.L. Graham, Can. J. Res., A25, 1 (1947).
5. H.G. Thode, et al., Advances in Inorganic Chemistry and Radiochemistry, H.J. Emeleus and A.G. Sharpe, editors, Academic Press, Inc., New York, 1960.
6. S. Katcoff, Nucleonics 18, 201-8 (1960).
7. O.R. Frisch, Nature 143, 276 (1939).
8. D.C. Brunton and G.C. Hannah, Can. J. Res. A28, 190 (1950).
9. D.C. Brunton and W.B. Thompson, Can. J. Res A28, 498 (1950).
10. F. Joliot, Compt. rend. 208, 341, 647 (1939).
11. M.C. Henderson, Phys. Rev. 58, 774 (1940).
12. R.B. Leachman and W.D. Schafer, J. Can. Phy. 33, 357 (1955).
13. R.B. Leachman, Phys. Rev. 83, 17 (1951).
14. R.B. Leachman, Phys. Rev. 87, 444 (1952).
15. J.K. Knipp and R.C. Ling, Phys. Rev. 82, 30 (1951).
16. H.W. Schmitt and R.B. Leachman, Phys. Rev. 102, 183 (1956).
17. R.B. Leachman and H.W. Schmitt, Phys. Rev. 96, 1366 (1954).
18. W.E. Stein, Phys. Rev. 108, 94 (1957).
19. W.E. Stein and S.L. Whetstone, Jr., Phys. Rev. 110, 476 (1958).
20. J.C.D. Milton and J.S. Fraser, Can. J. Phys. 40, 1626 (1962).
21. H.R. Bowman, et al., UCRL-9713-Rev (1961).
22. W.E. Stein and R.B. Leachman, Rev. Sci. Instr. 27, No. 12, 1049-50 (1956).

23. N.O. Lassen, Kgl. Danske Videnskab. Selskab, Mat. fys. Medd. 26, No. 5 (1951).

24. H.A. Bethe and J. Ashkin, Experimental Nuclear Physics, John Wiley & Sons, Inc., 251, Vol. I, New York, 1953.

25. E. Gatti and V. Svelto, Proc. Symp. Nuclear Instr., editor J.B. Birks, Academic Press, New York, 1962.

26. C.N. Winningstad, Wescon Paper (1961).

27. C.T. Kohn, Proc. I.R.E. 43, 951 (1955).

28. J.H. Neiler, ORNL-3268 (1962).

29. L. Beghian, G. Kegel, and R. Scharenburg, Rev. Sci. Instr. 29, 753 (1958).

30. E. Gatti and V. Svelto, Nuclear Instr. & Methods 4, 189 (1959).

31. J.H. Neiler, Fast Neutron Physics, edited by J.B. Marion and J.L. Fowler, Interscience Publishers, Inc., New York, 1960.

32. S.C. Lind, Radiation Chemistry of Gases, Reinhold Corp., 24, New York, 1961.

33. E. Rutherford and J. Chadwick, Radiations from Radioactive Substances, University Press, 151, Cambridge, 1930.

34. J.S. Fraser and J.C.D. Milton, Nuclear Instrs. 2, 275-81 (1958).

35. R.B. Leachman and H.W. Schmitt, Phys. Rev. 96, No. 5, 1366-71 (1954).

36. C.B. Fulmer, Phys. Rev. 108, 1113 (1957).

37. B. Diven, et al., Phys. Rev. 101, 1012 (1956).

38. R.W. Lide, ORNL-3338 (1962).

39. G. Bellettini, et al., Nuclear Instr. & Methods 21, 106-112 (1963).

40. A.E. Bjerke, et al., UCRL-9838 (August 1961).

41. E.J. Sternglass and M.M. Wachtel, IRE Trans. on Nuc. Sci. 29 (1956).

42. R.L. Chase, Nuclear Pulse Spectrometry, McGraw-Hill Book Co., Inc. New York, 1961.

43. W. Bartl and P. Weinzierl, Rev. Sci. Instr. 34, 252 (1963).

44. R.A. Shatas, J.F. Marshall, and M.A. Pomerantz, Phys. Rev. 96, 1199 (1954).

# APPENDIX A

## ANALYSIS OF THE TPHC OUTPUT CIRCUITRY

From Figure 16, vacuum tube V4 and its associated circuitry is reproduced below:

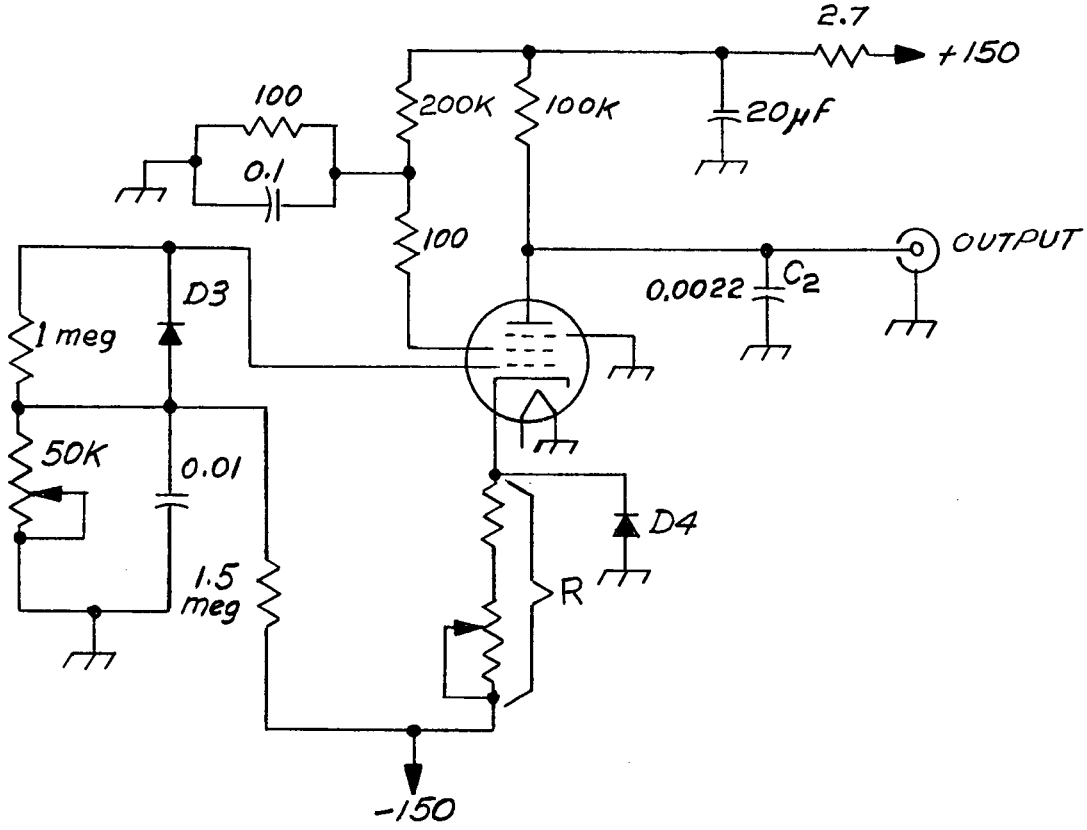


Let: $i_K$ = cathode current,

$i_p$ = plate current,

$i_o$ = quiescent current through R and diode D4 while V4 is non-conducting,

$g_m$ = tube transconductance,

$V_c$ = V4 cut-off potential with respect to ground,

$e_{g_o}$ = grid-to-ground signal,

$e_{g_K}$ = grid-to-cathode potential,

$V_{D4}$ = reverse bias potential of D4.

Assume: Since $R > R_L$ and $R_p$ (plate resistance), $R_L$ and $R_p$ are negligible.

Region (1): $i_p = 0$ when $e_{g_o} \leq V_c$, (72)

and $i_K = i_o$.

Region (2): $V_c < e_{g_o} < V_{D4}$.

Here $i_p^{(2)} > 0$, but $V_K < V_{D4}$, (73)

where: $V_K$ = cathode potential with respect to ground.

At all times in this region of operation,

$$i_p^{(2)}R = 150 - i_o'^{(2)}(R + R_{D4}), \tag{74}$$

where: $i_o'^{(2)}$ = current through diode D4 as the cathode potential of V4 rises,

= $i_o$ when $i_p = 0$,

$R_{D4}$ = effective resistance of Diode D4 and a function of $i_o'$.

$$i_k^{(2)} = i_p^{(2)} + i_o'^{(2)}. \tag{75}$$

$$i_p^{(2)} = g_m^{(2)}[e_{g_k}^{(2)} + V_c]. \tag{76}$$

$$e_{g_k}^{(2)} = e_{g_o}^{(2)} - V_c + 150 - i_k^{(2)} R. \tag{77}$$

Combining Equations (75), (76), and (77) yields,

$$i_p^{(2)} = \frac{g_m^{(2)}[e_{g_o}^{(2)} + \frac{150\ R_{D4}}{R + R_{D4}}]}{1 + g_m^{(2)} \frac{R_{D4}R}{R_{D4} + R}} . \tag{78}$$

Region (3): $e_g^{(3)} > V_{D4}$; diode D4 is reverse-biased. (79)

$$i_p^{(3)} > 0;\ i_k^{(3)} = i_p^{(3)} + i_o'^{(3)}.$$

But, $i_o'^{(3)} = 0$, by definition. (80)

$$i_p^{(3)} = g_m^{(3)}[e_{g_k}^{(3)} + V_c] . \tag{81}$$

$$e_{g_k}^{(3)} = e_{g_o}^{(3)} - V_c + 150 - i_k^{(3)} R ,$$

from which:

$$i_p^{(3)} = \frac{g_m^{(3)}[e_{g_o}^{(3)} + 150]}{1 + g_m^{(3)}R} . \tag{82}$$

The change in current between regions (2) and (3) is:

$$i_p^{(3)} - i_p^{(2)} = \Delta i_p .$$

$$\Delta i_p = (\frac{g_m R}{R_{D4}}) \frac{150 - g_m\ e_{g_o}^{(3)} R}{(1 + g_m R)(1 + \frac{g_m R\ R_{D4}}{R + R_{D4}})} , \tag{83}$$

where the assumptions have been made that:

(1) $e_{g_o}^{(2)} = e_{g_o}^{(3)}$,

(2) $g_m^{(2)} \simeq g_m^{(3)}$.

Equation (83) indicates that there is a decrease in current between the two regions. Since the grid-to-ground signals and biases change from tube to tube, it is difficult to establish an absolute limit for this current change. However, since the total change in current from region (1) to region (3) is limited to 150 μamps, Equation (83) indicates $\Delta i_p$ is extremely small and varies with $e_{g_o}^{(3)}$. The slope of the current with respect to $e_{g_o}$ for regions (2) and (3) is:

$$\frac{di_p^{(2)}}{de_{g_o}^{(2)}} = \frac{g_m^{(2)}}{1 + g_m^{(2)} \frac{R_{D4} R}{R_{D4} + R}} \sim g_m^{(2)}, \tag{84}$$

$$\frac{di_p^{(3)}}{de_{g_o}^{(3)}} = \frac{g_m^{(3)}}{1 + g_m^{(3)} R} \sim \frac{1}{R} \approx 0. \tag{85}$$

The slope of the current change with respect to $e_{g_o}^{(3)}$ is, from Equation (83):

$$\frac{d\Delta i_p}{de_{g_o}^{(3)}} \simeq - \frac{(g_m R)^2}{R_{D4}} . \tag{86}$$

A plot of $i_p$ versus $e_{g_o}$ illustrates the operation of the constant current tube:

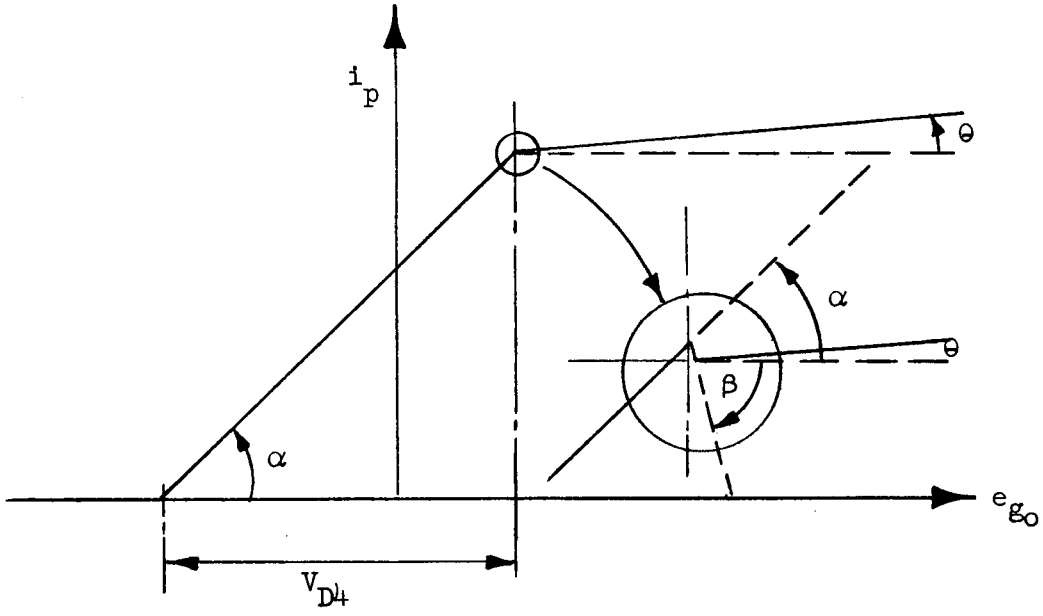


Characteristic Curve for TPHC Output Circuit

$$\theta = \tan^{-1} \frac{1}{R};$$

$$\theta = 0.$$

$$\alpha \sim \tan^{-1} g_m^{(2)}.$$

$$\beta \sim \tan^{-1} - \frac{(g_m R)^2}{R_{D4}}.$$

$V_{D4}$ = reverse bias potential of diode D4.

Note: The curve is illustrated by straight lines to emphasize the relatively abrupt plate current change when D4 becomes reverse-biased.

# APPENDIX B

## THE DISTRIBUTION OF TIME INTERVALS FORMED BETWEEN A FIXED-FREQUENCY PULSER AND A RANDOM TIME SOURCE AS MEASURED BY THE TPHC

Let:

$n$ = number of pulses occurring at any instant in a time interval $\delta t$,

$\bar{n}$ = average number of pulses in the time interval $\delta t$,

$N$ = total number of pulses available,

$T$ = total time interval during which N pulses occur.

Then:

$$\bar{n} = \frac{N}{T}(\delta t), \tag{87}$$

or

$$\frac{\bar{n}}{\delta t} = \frac{N}{T}. \tag{88}$$

Define:

$$g \equiv \frac{\delta t}{T}, \tag{89}$$

for $g \ll 1$, $T \gg \delta t$.

The probability of a fluctuation in which "n" pulses occur in a time interval $\delta t$ is given by the Binomial Distribution:

$$p_n = \frac{N!}{n!(N-n)!} g^n (1-g)^{N-n}. \tag{90}$$

For the case in point, $g \gg 1$, i.e., $T \ll \delta t$ and $N \gg 1$ and $N \gg n$, the Binomial Distribution yields the Poisson Distribution:

$$p_n \simeq \frac{e^{-\bar{n}} \bar{n}^n}{n!}. \tag{91}$$

Note that Equation (91) is independent of "n"; there is no condition imposed on n except that $N \gg n$; and $\bar{n} \equiv Ng$.

For:

$$n = 0,\ P_o = e^{-\bar{n}},$$

$$n = 1,\ P_1 = e^{-\bar{n}}\,\bar{n}, \tag{92}$$

$$n = 2,\ P_2 = e^{-\bar{n}}\,\frac{\bar{n}^2}{2},$$

$$n = i,\ P_i = e^{-\bar{n}}\,\frac{\bar{n}^i}{i!}.$$

The question is now raised of what is the probability for obtaining <u>at least</u> one pulse in any interval $\delta t$ when the average number of pulses is $\bar{n}$.

Here: $P(\geq 1)$ = the probability of obtaining 1 count, 2 counts, 3 counts, etc. in the interval $\delta t$,

$$= P(1) + P(2) + P(3) + \ldots + P(N). \tag{93}$$

$$P(\geq 1) = \sum_{n=1}^{N} P_n,$$

$$= \sum_{n=1}^{N} e^{-\bar{n}}\,\frac{(\bar{n})^n}{n!},$$

$$= e^{-\bar{n}} \sum_{n=1}^{N} \frac{(\bar{n})^n}{n!} = \left[e^{-n} \sum_{n=0}^{N} \frac{(\bar{n})^n}{n!}\right] - e^{-\bar{n}}. \tag{94}$$

If $N \gg 1$ and $N \gg n$, as has been assumed, then with negligible error, $N \to \infty$ in the summation since the terms for $n > N$ in the summation contribute little if anything to the sum.

Hence:

$$\sum_{n=0}^{n=N} \frac{(\bar{n})^n}{n!} \to \sum_{n=0}^{\infty} \frac{(\bar{n})^n}{n!} \equiv e^{\bar{n}}. \tag{95}$$

Equation (94) becomes:

$$P(\geq 1) = e^{-\bar{n}}(e^{\bar{n}} - 1), \tag{96}$$

$$= 1 - e^{-\bar{n}},$$

= probability of obtaining at least one count in any time interval $\delta t$.

Now, given m channels, each $\delta t$ in width such that $m(\delta t) = T$, how will the available N pulses be distributed throughout the channels if channel occupancy is noted when at least one pulse arrives in that channel?

The answer to this query is supplied by Equation (96) which shows that since the time intervals $\delta t$ (taken here to be equal, for convenience) are mutually independent, then , for a given n, the distribution is constant.

As $\bar{n} \to \infty$, $P(\geq 1) = 1$ (certainty).

As $\bar{n} \to 0$, $P(\geq 1) = 0$ (impossibility).

Equation (96) could have been deduced much more simply by noting that:

$$P_n = 1 = \Sigma[P(0) + P(\geq 1)], \tag{97}$$

$$P(0) = e^{-\bar{n}};$$

$$\therefore \quad P(\geq 1) = 1 - e^{-\bar{n}}. \tag{98}$$

However, the real question is this: If the channels are ordered, how will the "N" pulses be distributed if channel occupancy is noted when <u>at least</u> one pulse arrives in that specific channel?

This question imposes a conditional probability in that the occupancy of the $i^{th}$ channel requires vacancies in the preceding $(i - 1)$ channels.

Let: $P(i)$ = probability for $i^{th}$ channel occupancy,

$Q(i-1)$ = probability for $(i-1)^{th}$ channel vacancy,

but $Q(i-1) = 1 - P(i)$. (99)

$$\therefore \quad P(i)Q(i-1)^{(i-1)} = P(i)[1 - P(i)]^{(i-1)}, \tag{100}$$

= probability of $i^{th}$ channel occupancy with the preceding $(i-1)$ channels vacant.

Now, $P(i) = 1 - e^{-\bar{n}}$ from Equation (96).

$$\therefore \quad P[\geq 1, i, P(i)] = (1 - e^{-\bar{n}})(e^{-\bar{n}})^{(i-1)}, \tag{101}$$

$$= e^{-\bar{n}i}(e^{\bar{n}} - 1) .$$

Equation (101) clearly shows the channel dependence of the distribution function.

Compare the $i^{th}$ channel with the $(i-1)^{th}$ channel occupancy probability:

$$\frac{e^{-\bar{n}(i+1)}(e^{+\bar{n}} - 1)}{e^{-\bar{n}i}(e^{\bar{n}} - 1)} = e^{-\bar{n}}. \tag{102}$$

Equation (102) shows that adjacent channel probabilities differ by this factor.

Comparing the 1st channel occupancy with the $m^{th}$ channel occupancy probability yields:

$$\frac{e^{-m\bar{n}}(e^{\bar{n}} - 1)}{e^{-\bar{n}}(e^{\bar{n}} - 1)} = e^{-m\bar{n}+\bar{n}}, \tag{103}$$

$$= e^{\bar{n}(1-m)}.$$

For $m \gg 1$, which is surely the case for a 512 channel analyzer where $m = 512$,

$$e^{\bar{n}(1-m)} \rightarrow e^{-m\bar{n}} . \tag{104}$$

Equation (104) shows the channel number dependency in the distribution function.

For a direct application of these results to this time-of-flight apparatus,

$$\bar{n} = r\,\delta t,$$

where: $r$ = average random source counting rate.

$$\delta t = \frac{T_o}{m},$$

where: $T_o$ = 633.95 nsec,

$m$ = channel number, at least greater than 10;

$$\therefore \quad e^{-m\bar{n}} = e^{-r\,T_o},$$

for $r$ = 3500 counts/sec,

and $T_o = 633.95 \times 10^{-9}$ sec,

$$e^{-rT_o} \rightarrow e^{-1.9 \times 10^{-3}} \sim 1 . \tag{105}$$

which indicates that the distribution of time intervals between a fixed frequency generator (used as Start signals) and random signals due to a radioactive source of rate r as listed above (used as Stop signals) is flat, i.e., random.

# APPENDIX C

## CHANCE COINCIDENCE RATES IN A TRIPLE COINCIDENCE SYSTEM

In a double time-of-flight apparatus, the slow coincidence constraint involves three signals; hence, it is of interest to determine the accidental triple coincidence counting rate. For simplicity, consider each detector as having the same resolving time, $\tau$, and receiving uncorrelated signals at counting rates $n_o$, $n_1$, and $n_2$, respectively.

For the zero detector and #1 detector, the following situation accrues. All signals from the zero detector which arrive at the coincidence circuit and are separated from a #1 detector signal arriving at the same circuitry by a time interval less than $\tau$ are recorded as accidental or chance coincidences. Each zero detector signal so scored must fall within one of a set of time intervals each of length $2\tau$ which is associated with the #1 detector signals and is assumed to be symmetrically oriented on either side of them. These time intervals equal a fraction $2\tau n_o$ of the total time of data collection. It is assumed also that this fraction is small, so that only an insignificant number of these time intervals overlay. Multiplying this fraction of time by $n_1$ (counting rate in detector #1) yields the accidental or chance coincident rate:

$$N_{A_2} = 2\tau n_o n_1 . \tag{106}$$

This chance coincident rate is distinguished from the true coincident rate which is:

$$N_c = N \omega_o \omega_1 \epsilon_o \epsilon_1 ,$$

where: $N_c$ = true coincidence rate,

$N$ = counting rate of true events,

$\omega_i$ = geometry factor for detector i; i = 0, 1,

$\epsilon_i$ = efficiency factor for detector i; i = 0, 1.

Following Chase,[42] consider each input signal as occupying a time interval equal to the circuit resolving time; therefore, when input signals are close enough for their associated time intervals to overlap, they record as being coincident. For multiple signals, an overlap of all their associated time intervals constitutes a coincidence; hence, consider now the three detectors of the time-of-flight apparatus. Since the counting rates $n_o$, $n_1$, and $n_2$ refer to uncorrelated events, all of the possible overlap times are equally likely; hence, if each associated time interval is of length $\tau$, the average length of the overlap intervals is $\frac{\tau}{2}$. Any #2 detector signals which occur during these overlap intervals or precede (or follow) them by less than $\tau$ are recorded as coincident with them. The average time interval during which a #2 detector signal yields a triple coincidence is:

$$\tau + \frac{\tau}{2} = \frac{3\tau}{2} . \tag{107}$$

The product of this average time interval and the chance coincident rate between the zero detector and #1 detector is:

$$(\frac{3\tau}{2})\ 2\tau\ n_o n_1 = 3\tau^2\ n_o n_1 . \tag{108}$$

Equation (108) gives the fraction of the data collection time during which #2 detector signals are recorded as coincident; from this, the triple chance coincidence rate is obtained by multiplying this fraction by $n_2$.

$$N_{A_3} = 3\tau^2 n_o n_1 n_2. \tag{109}$$

With short resolving times, the triple chance coincidence counting rate is negligible since the resolving time appears as a squared term.

But other conditions can yield triple chance coincidence rates which may not be negligible; e.g., a true double coincidence between any two detectors can be matched with a chance signal from the remaining third detector.

Let $N_{T_\alpha}$ = double coincidence rate for true events between any two detectors,

$n_{R.R.}$ = random counting rate of the third detector.

Following the arguments presented above, the fraction of the total time of data collection is $2\tau N_{T_2}$ based on the assumption that the detector signals occupy a time interval equal to its circuit resolving time. Multiplying this fraction of time by $n_2$ (counting rate in detector #2) yields the chance triple coincidence rate:

$$(2\tau\ N_{T_2})n_2 = N_{A_{3,T_2}}, \tag{110}$$

where: $N_{A_{3,T_2}}$ = chance triple-coincidence rate due to a true double coincidence and a random third detector signal.

Equation (110) is interesting, for it contains the resolving time to the first power [See Equation (109)]; however, with a low true double-coincidence rate, the weight attached to Equation (110) is also small.

For the time-of-flight apparatus used in this experiment,

$\tau \sim 0.5\ \mu\text{sec},$

$N_c \sim 13$ counts/sec,

$n_o \sim 6000$ counts/sec,

$n_1 \sim 5$ counts/sec,

$n_2 \sim 5$ counts/sec.

From which,

$$N_{A_2} = (2)(0.5 \times 10^{-6})(6 \times 10^3 \text{counts/sec})(5 \text{ counts/sec}), \quad (111)$$
$$= 3 \times 10^{-2} \text{ counts/sec.}$$

$$N_{A_3} = (3)(0.06 \times 10^{-12} \text{ sec}^2)(6 \times 10^3 \text{ c/sec})(5 \text{ c/sec})(5 \text{ sec}),$$
$$\cong 30 \times 10^{-9} \text{ counts/sec.} \quad (112)$$

$$N_{A_{3,T_2}} = (2)(0.5 \times 10^{-6})(13)(5) \text{ c/sec}, \quad (113)$$
$$= 65 \times 10^{-6} \text{ counts/sec.}$$

Note that $N_{A_{3,T_2}}$ refers to the following combinations of a true double coincidence and a chance third:

| Detector | Zero | #1 | #2 | |
|---|---|---|---|---|
| Case I | T | T | F | T = true |
| Case II | T | F | T | F = false |
| Case III | F | T | T | |

Cases I and II are more likely to occur than Case III because a true or real event in detector #2 presumes that the fission fragment had to traverse the zero detector Ni foil. This consideration excludes the effects of detector efficiency. Equation (113) is therefore to be multiplied by a factor of three to set an upper limit to $N_{A_{3,T_2}}$; hence,

$$3N_{A_{3,T_2}} = 195 \times 10^{-6} \text{ counts/sec.} \quad (113')$$

Three additional cases suggest themselves; viz.,

| Detector | Zero | #1 | #2 |
|---|---|---|---|
| Case IV | F | F | T |
| Case V | F | T | F |
| Case VI | T | F | F |

Cases IV and V represent the situation of a chance double coincidence with a true third signal. The chance double rate is given by Equation (106); however, with the true counting rate of 13 counts/sec at the remote detectors for this experiment, Cases IV and V are also negligible. Case VI is given by Equation (106) but with the true counting rate in the zero detector equal to 6000 counts/sec.

The sum of all these chance coincident rates represents a negligible contribution to the real counting rate for triple-coincidence true events.

# APPENDIX D

## FIGURES

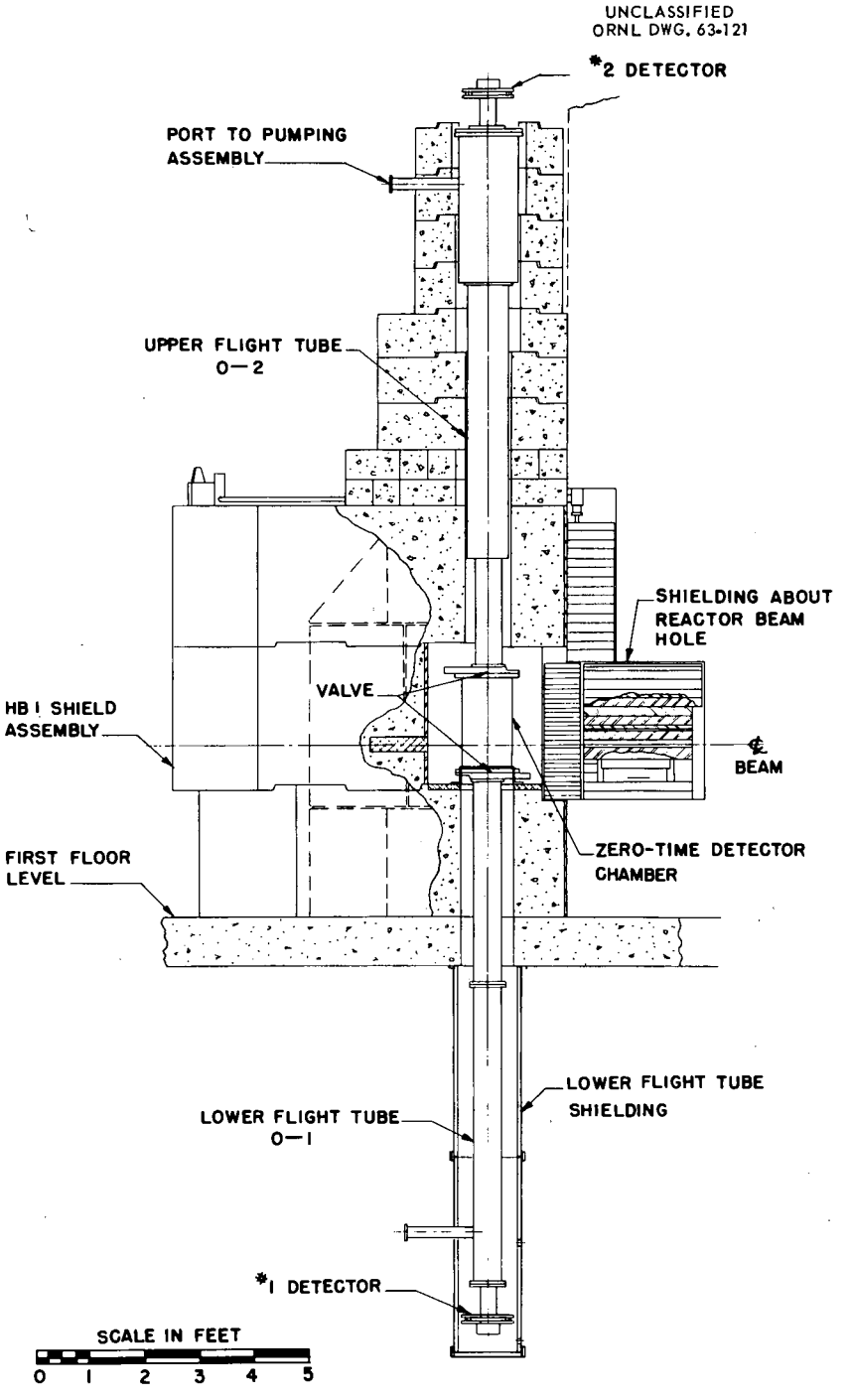


Figure 1. Schematic Diagram of Time-of-Flight Apparatus.

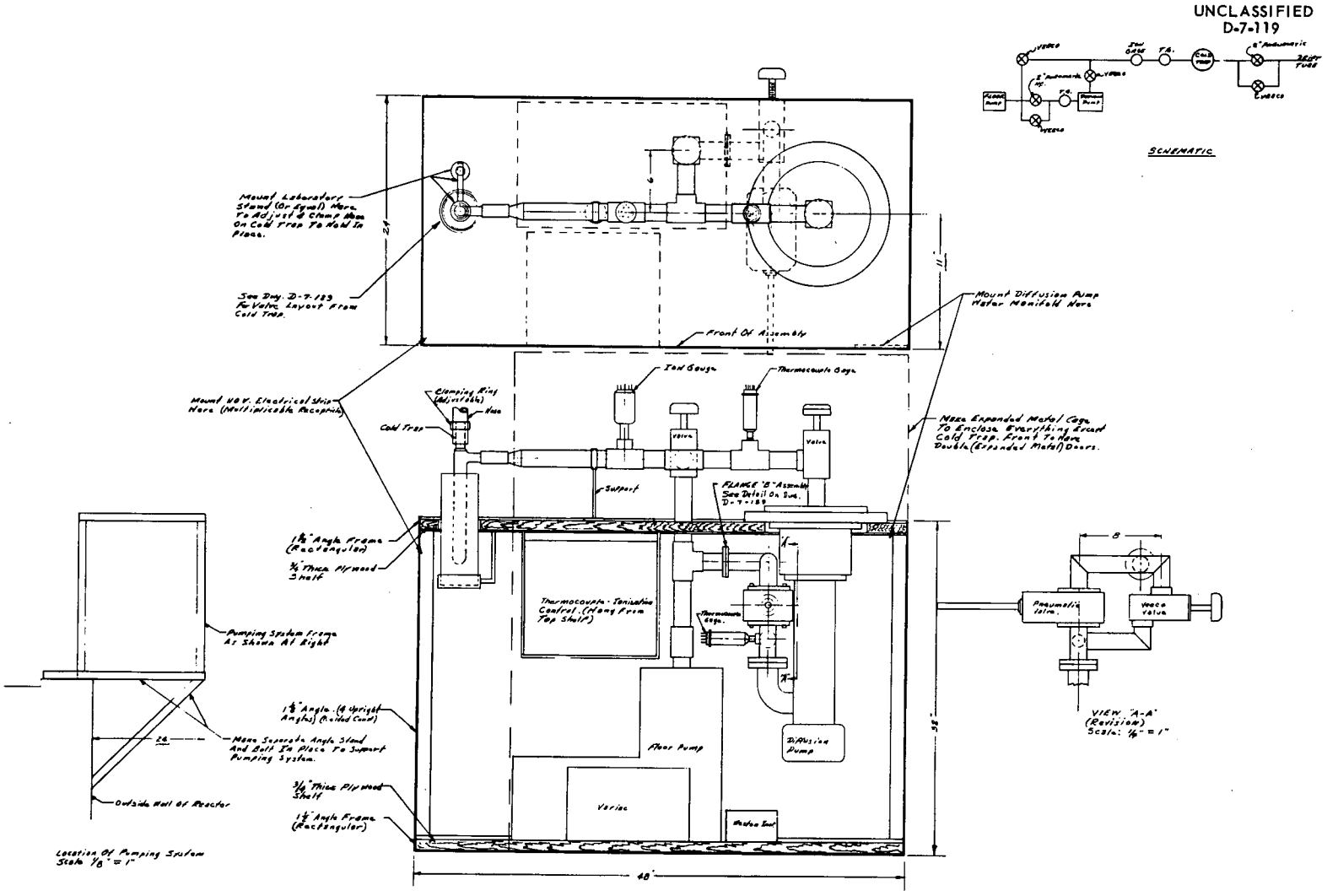


Figure 2. Typical Vacuum Station.

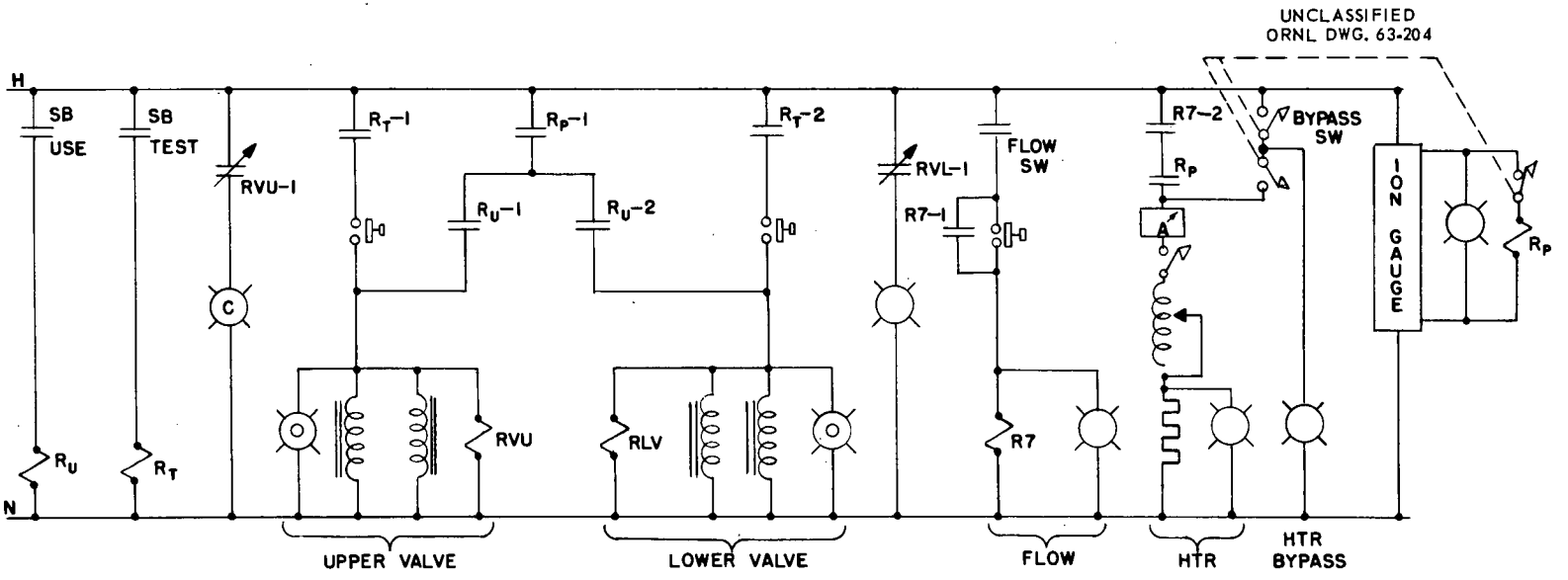


Figure 3. Instrumentation and Controls Diagram for Vacuum Stations.

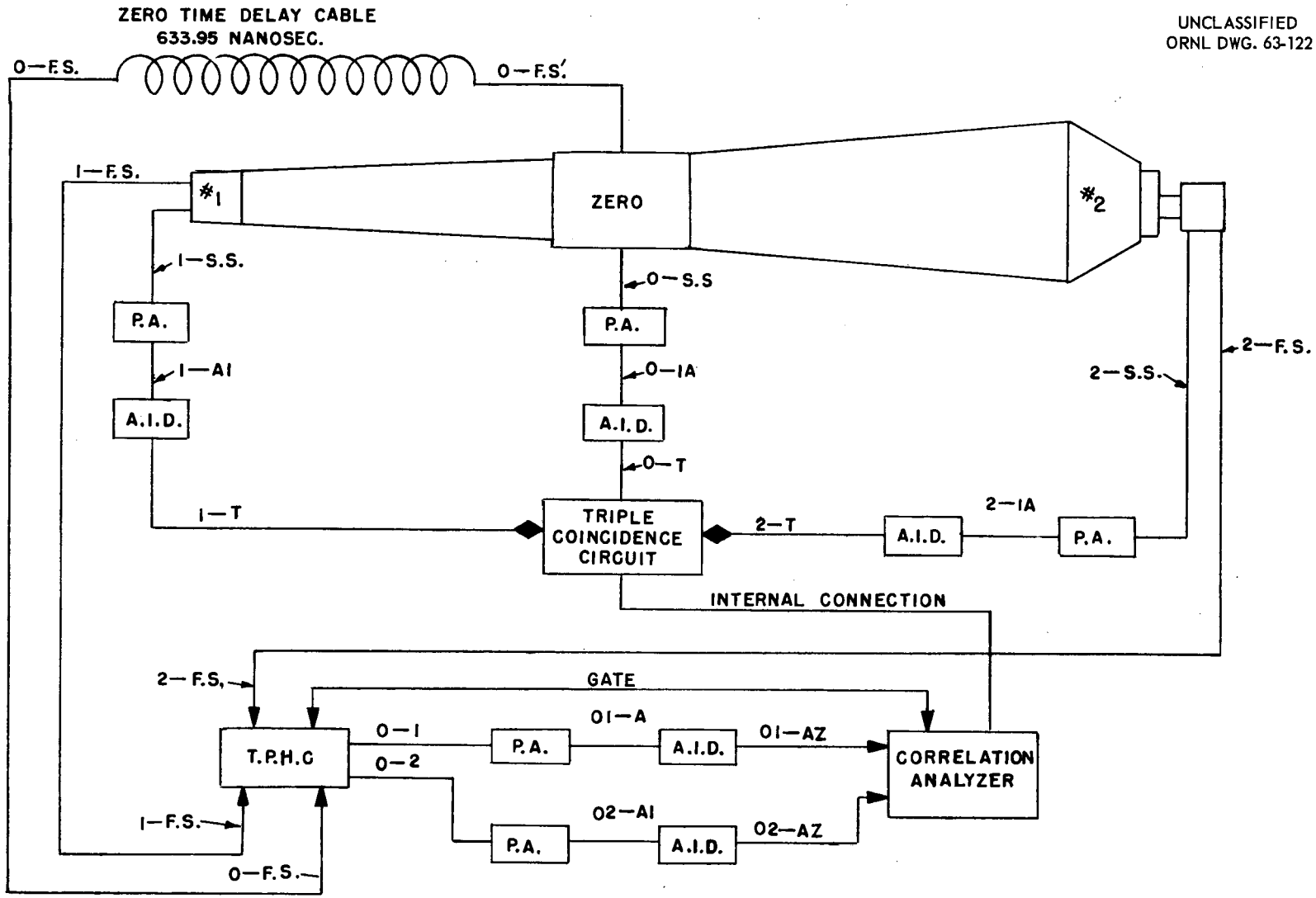


Figure 4. Block Diagram of the Time-of-Flight Electronics System.

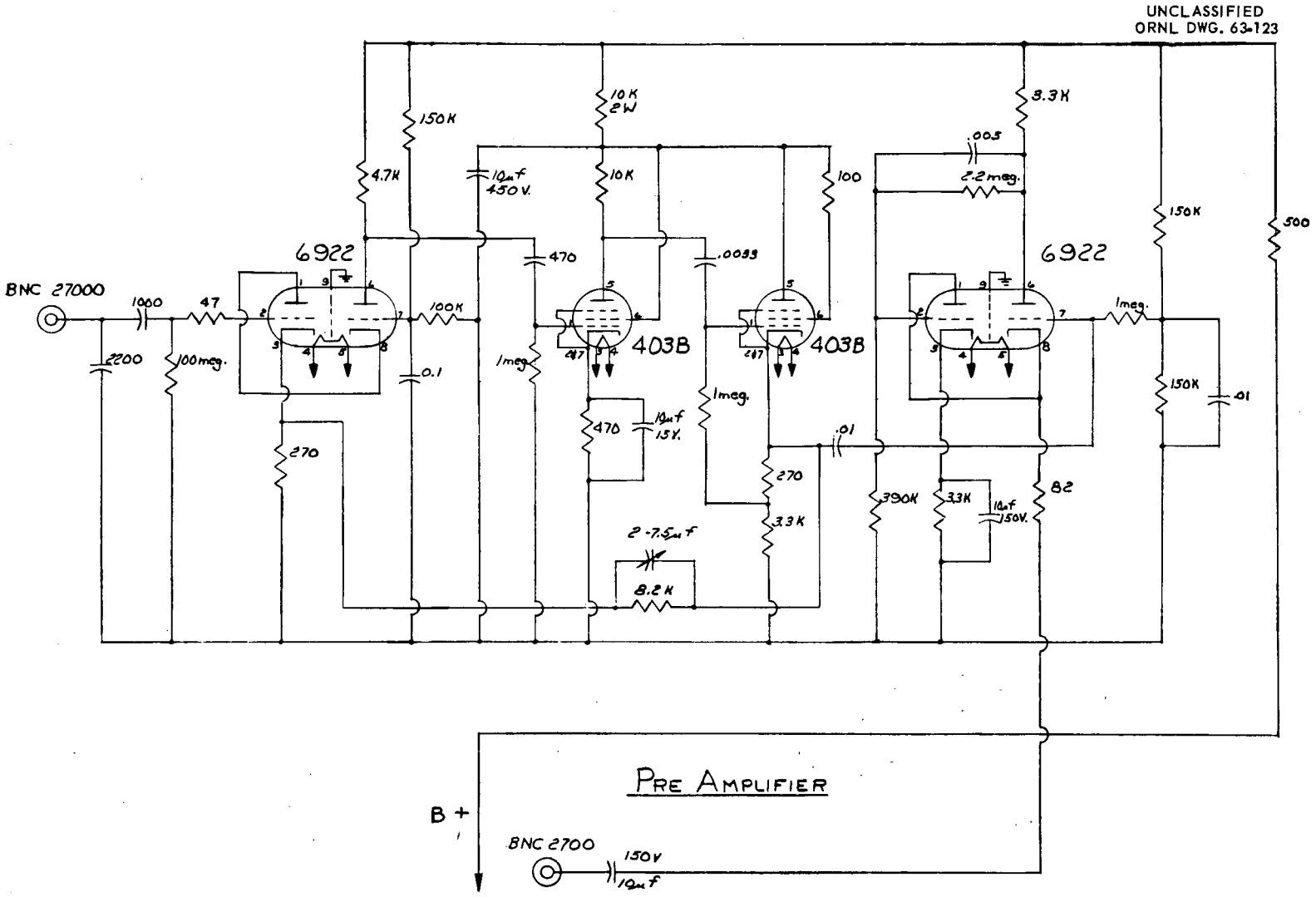


Figure 5. Schematic Diagram of the White Cathode-Follower Pre-Amplifier.

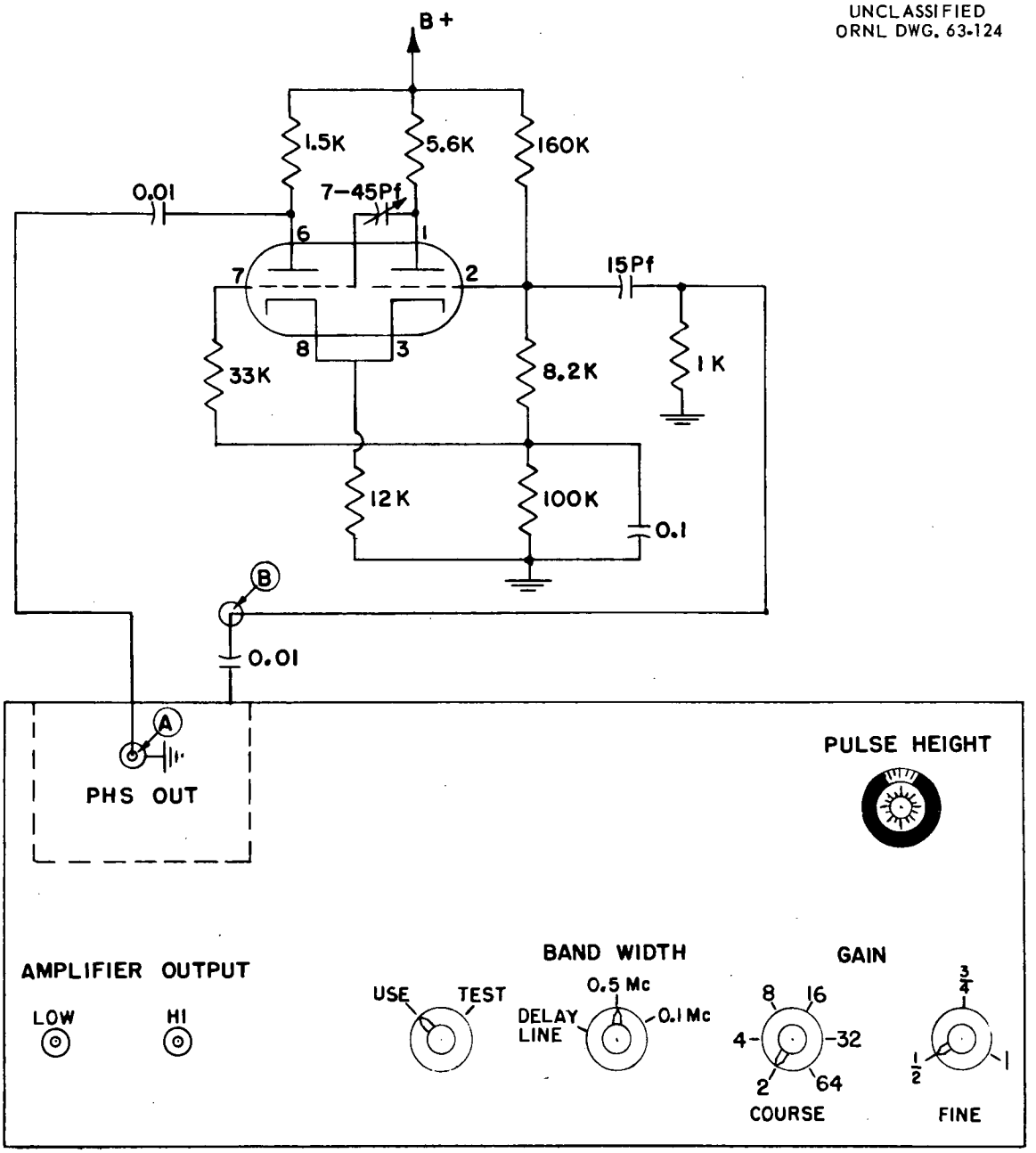


Figure 6. Schematic Diagram of Modified Pulse-Height Selector of a Standard A-1 Amplifier.

UNCLASSIFIED
ORNL DWG. 63-125

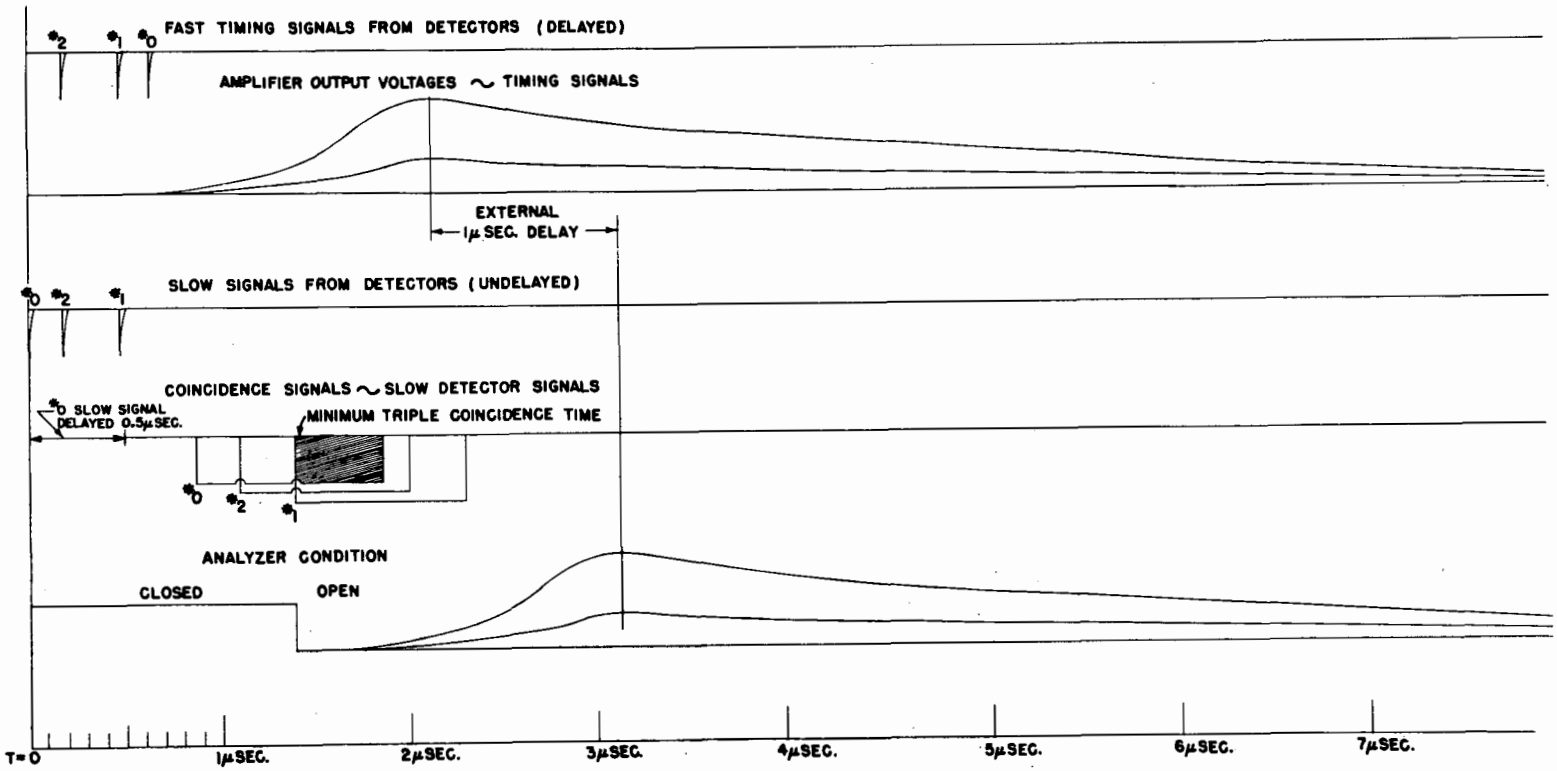


Figure 7. Time Sequence of the Pulses in the Double Time-of-Flight Apparatus.

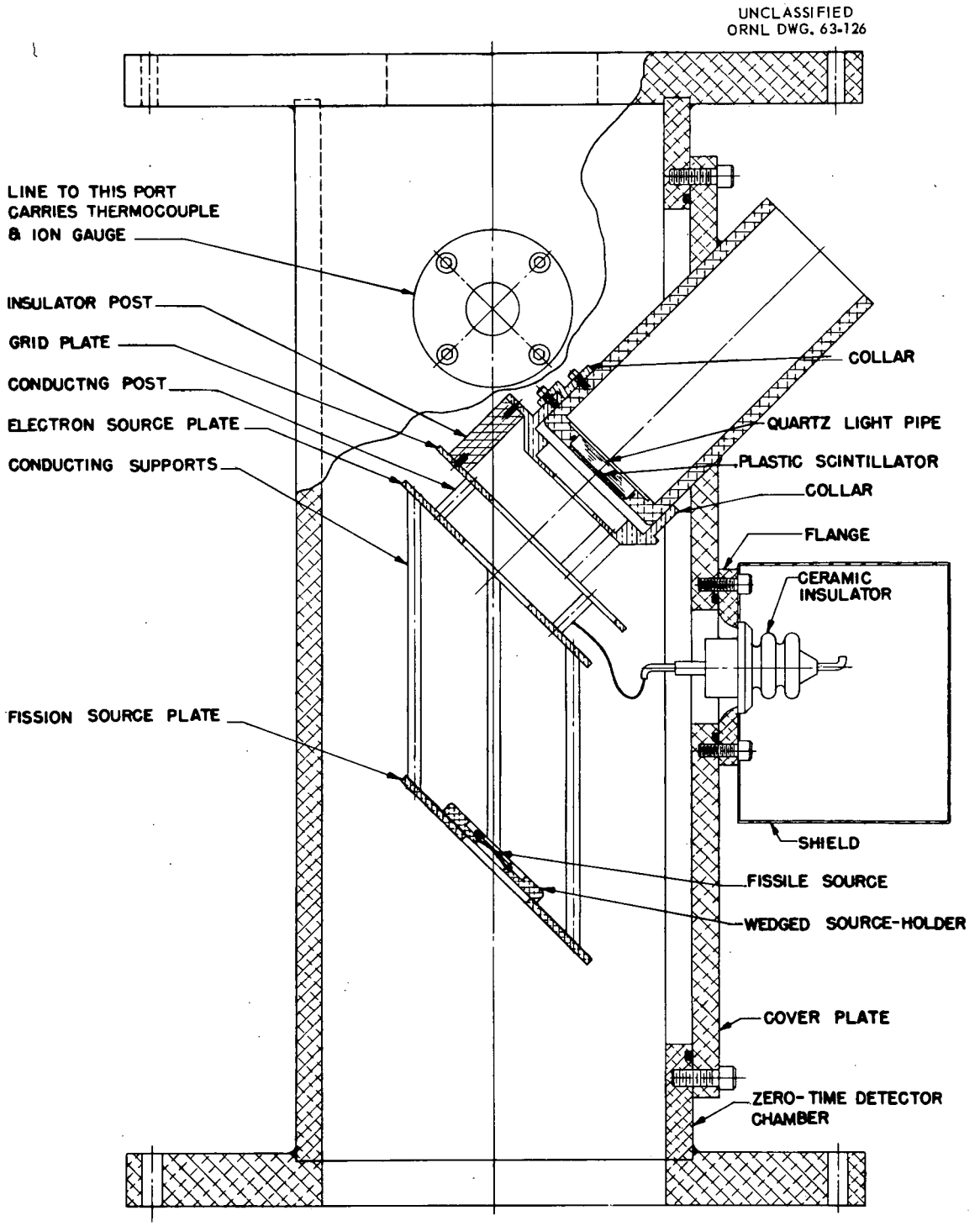


Figure 8. Zero Time Detector.

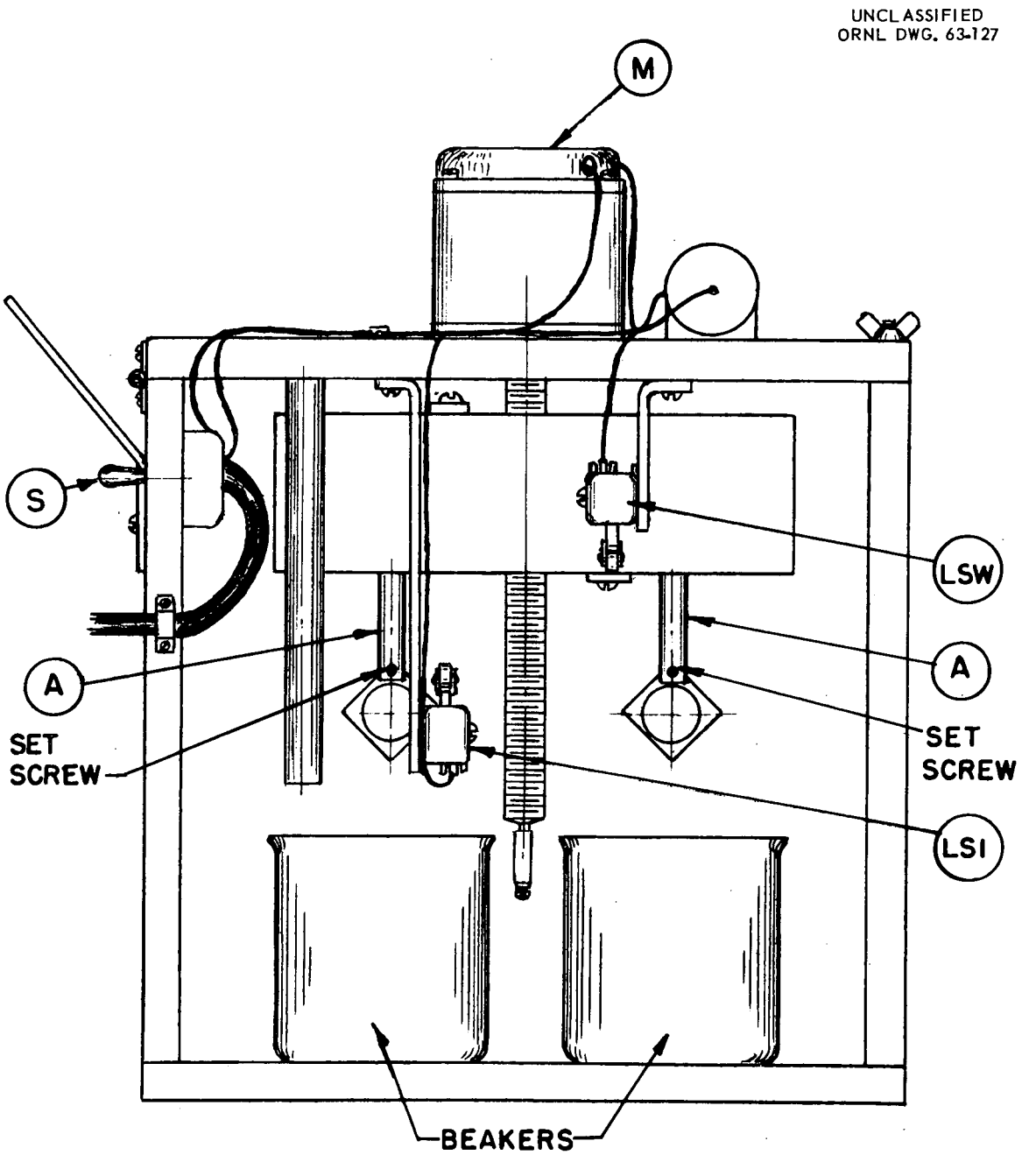


Figure 9. Foil Processor.

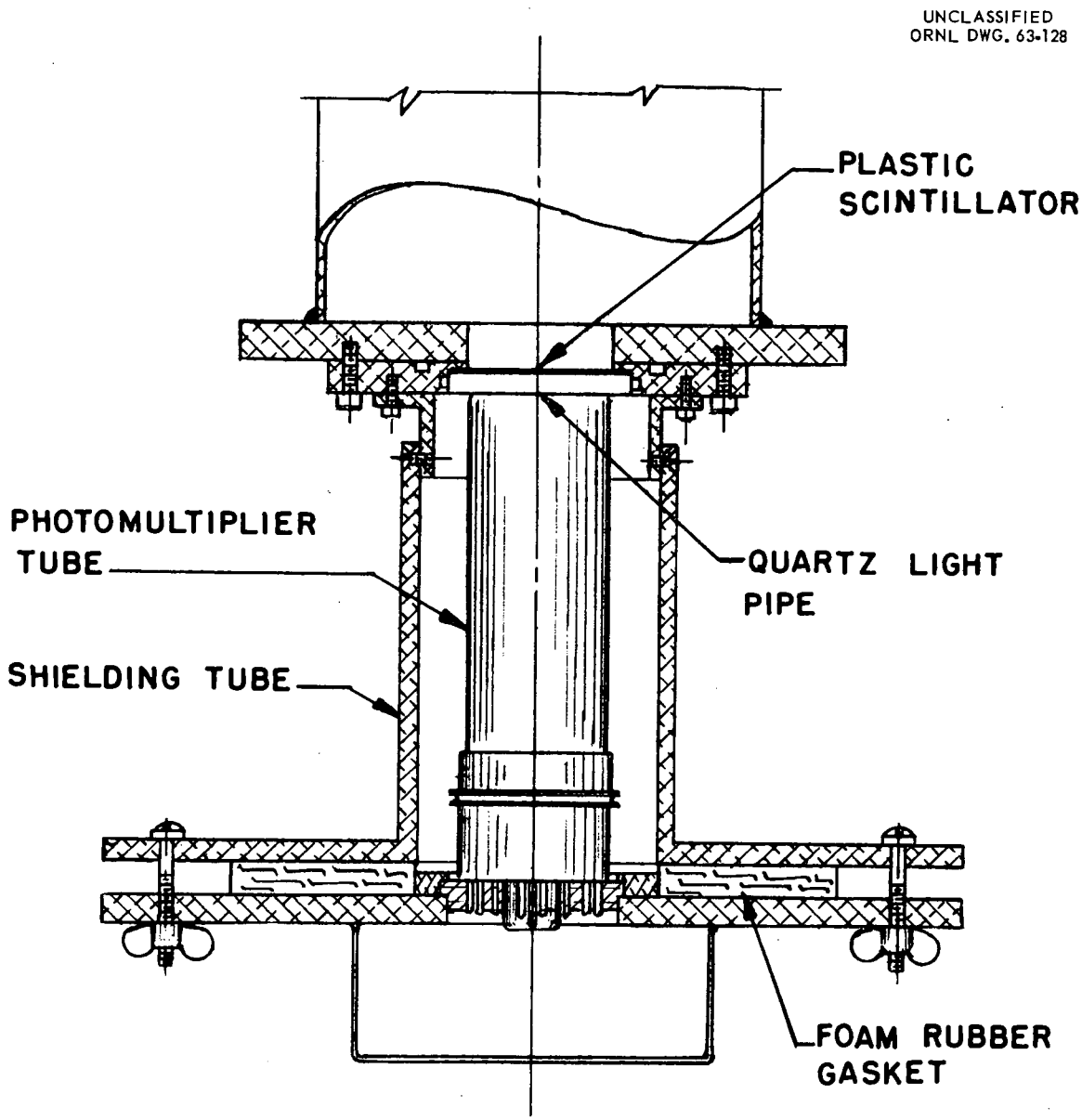


Figure 10. Typical Remote Detector.

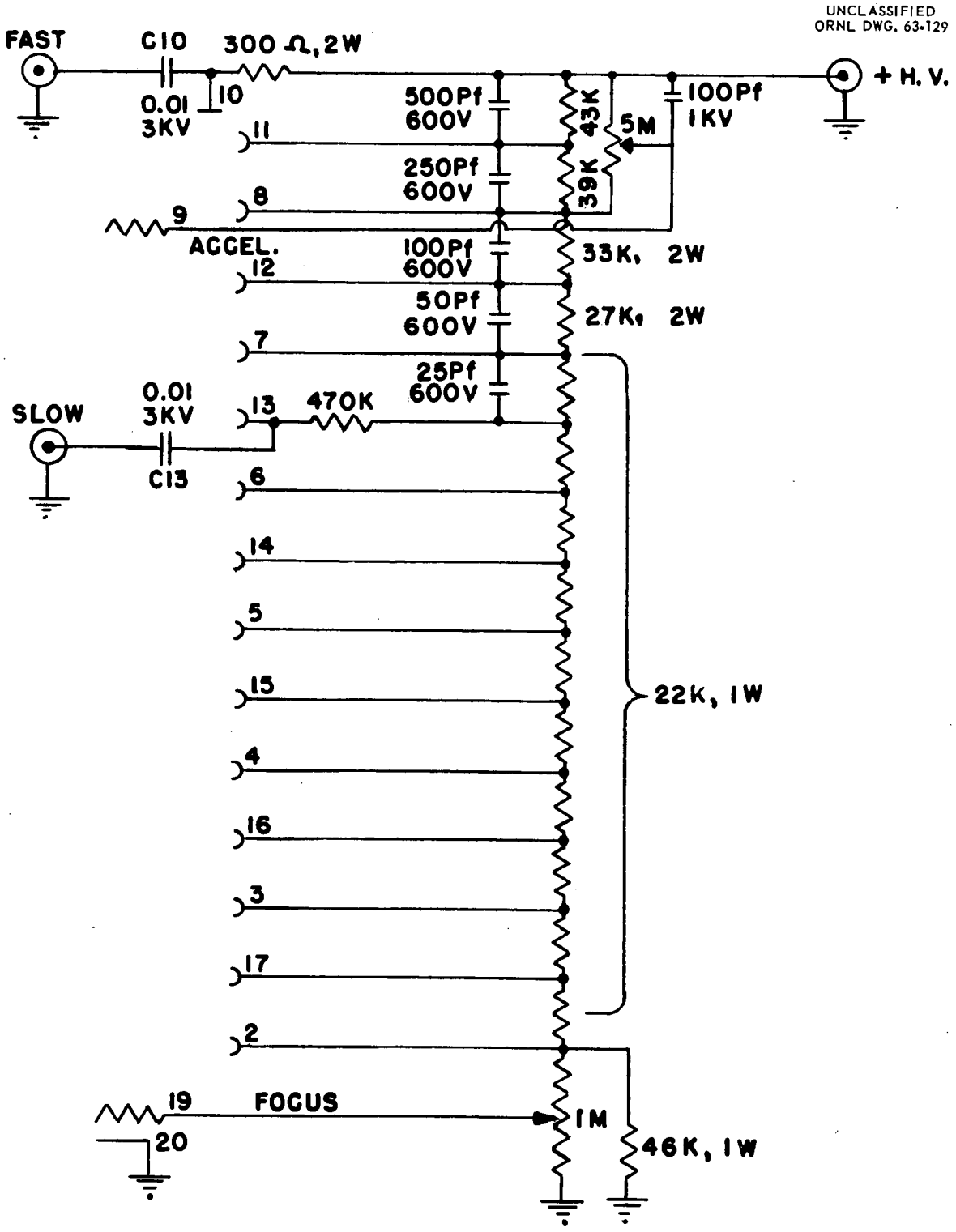


Figure 11. Detector Voltage Divider Network.

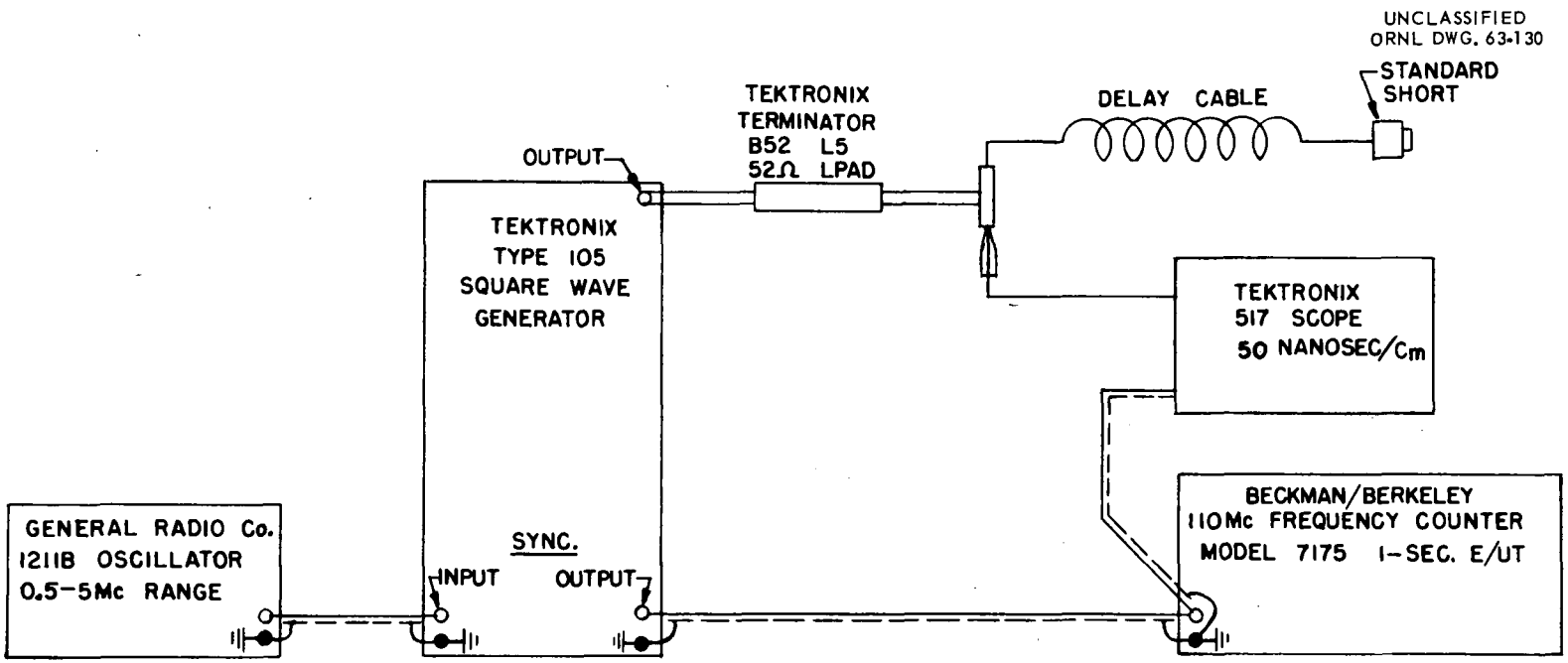


Figure 12. Schematic Diagram for Measuring Cable Delay Time.

UNCLASSIFIED
ORNL DWG. 63-131

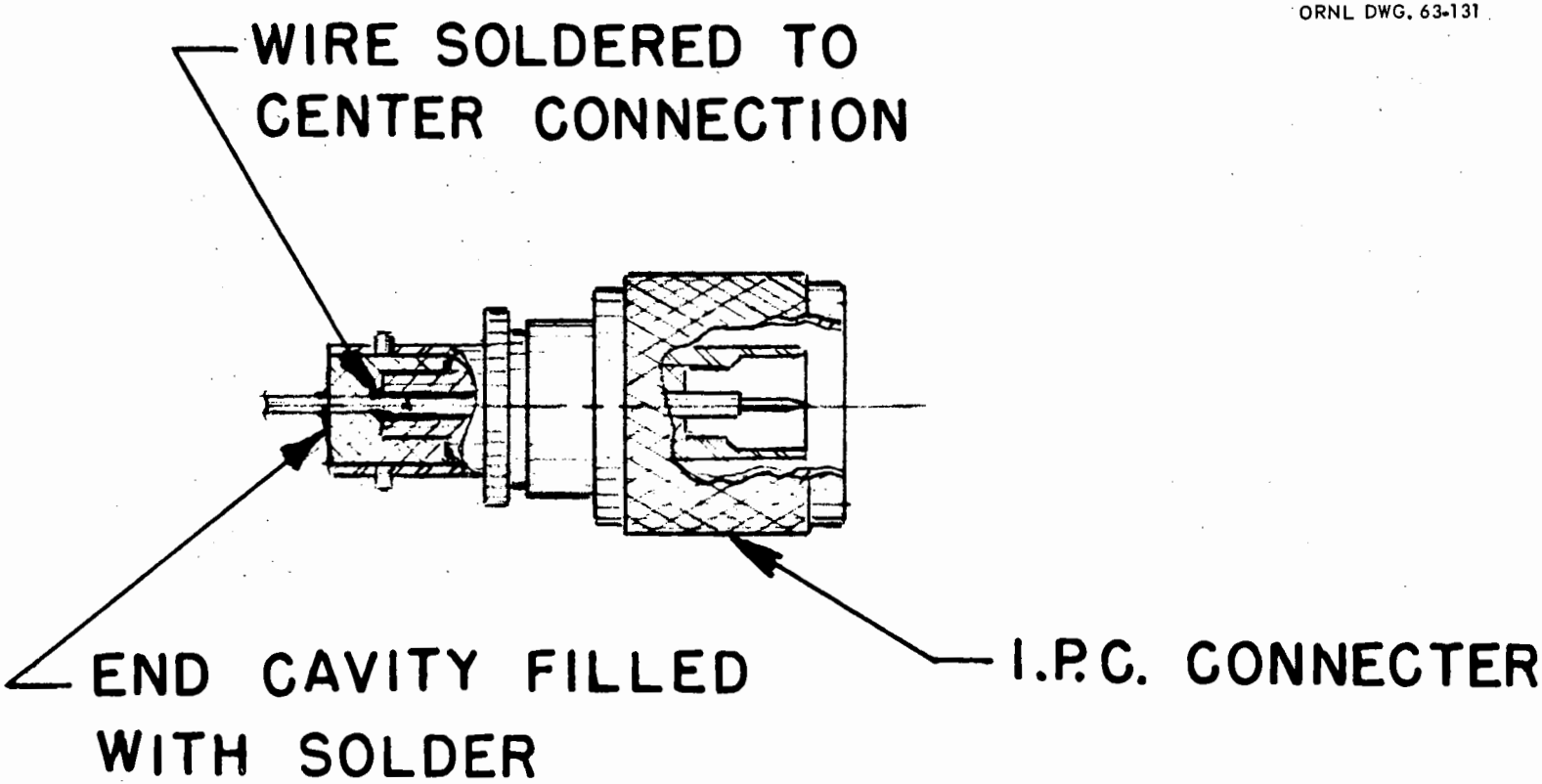


Figure 13. Standard Cable Terminator.

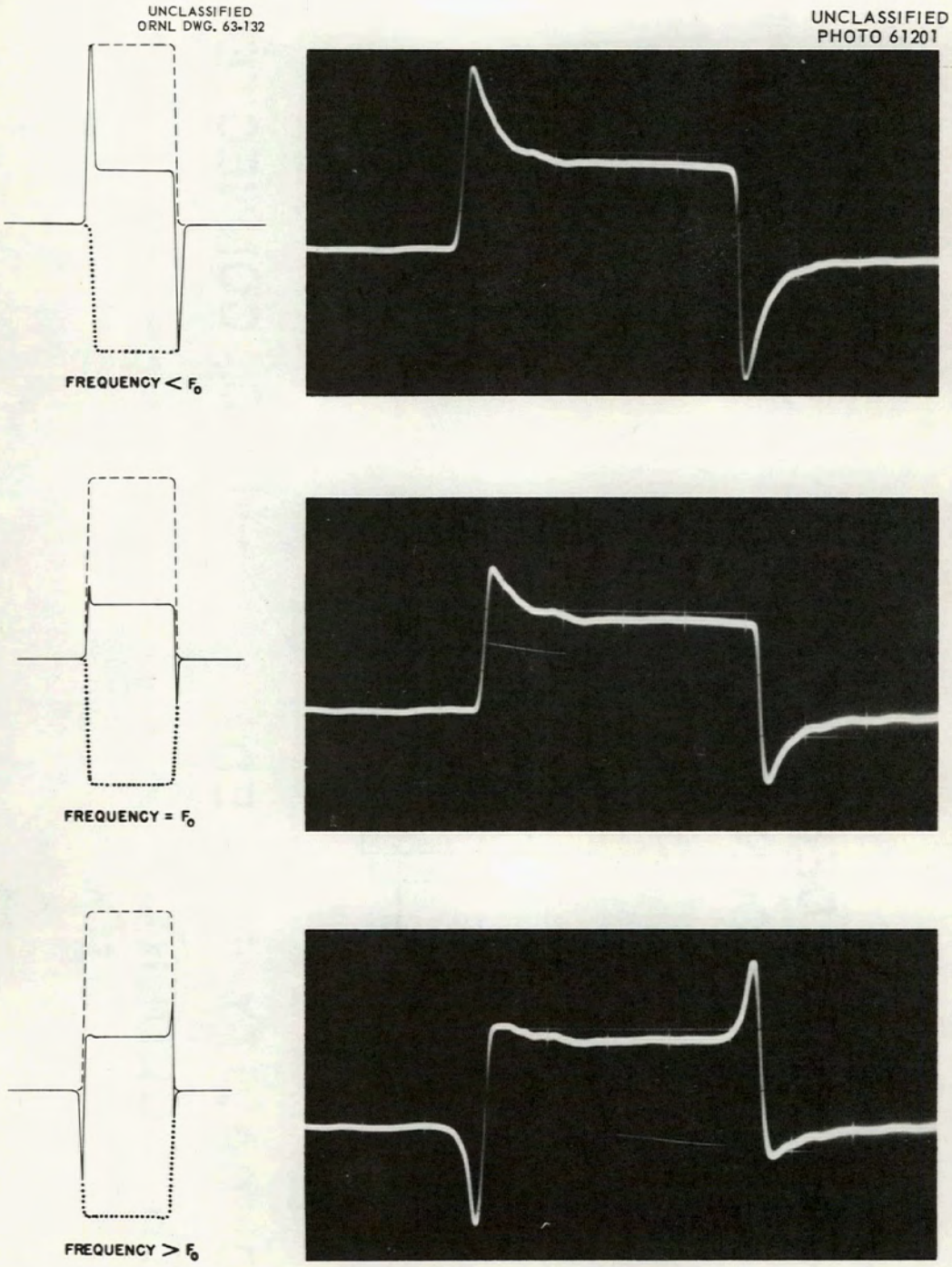


a. Graphical Display of Resultant Waveshapes Encountered in Cable Calibration.

b. Photographs of Oscilloscope Waveshapes Corresponding to Figure 14a.

Figure 14. Resultant Waveshapes in Cable Calibrations.

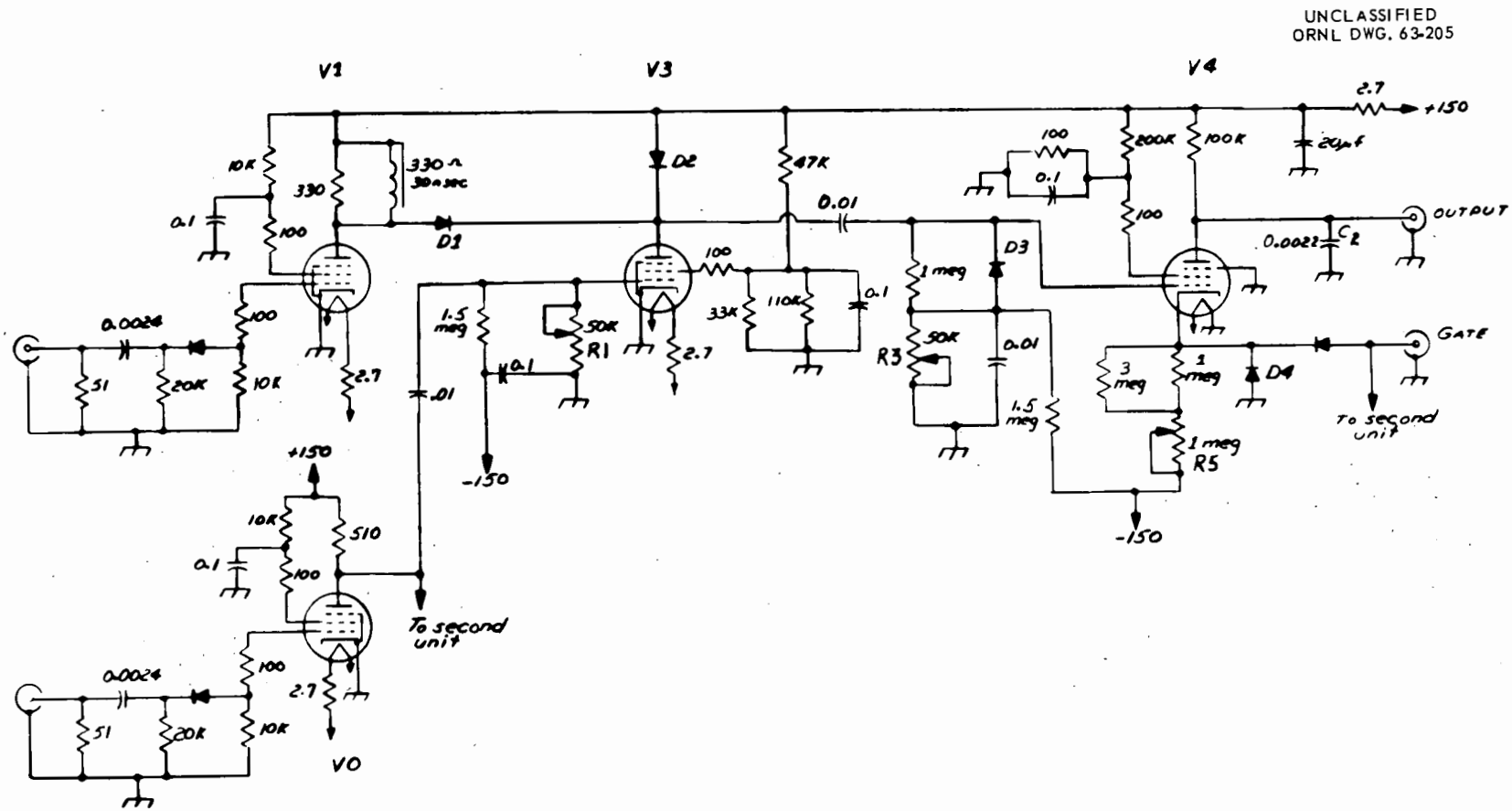


Figure 15. Time-to-Pulse-Height Converter.

UNCLASSIFIED
PHOTO 61202

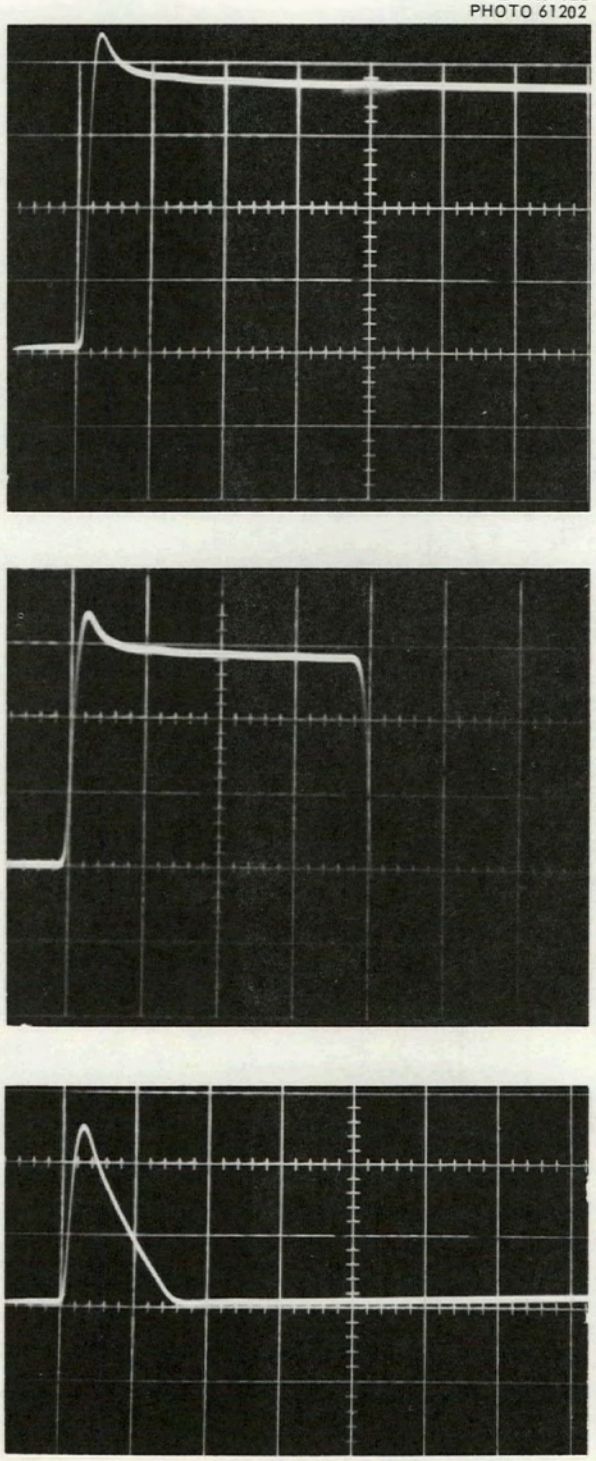

Figure 16. Photographs of Typical Diode-Stretcher Voltage Shapes in the Time-to-Pulse-Height Converter.

UNCLASSIFIED
PHOTO 61200

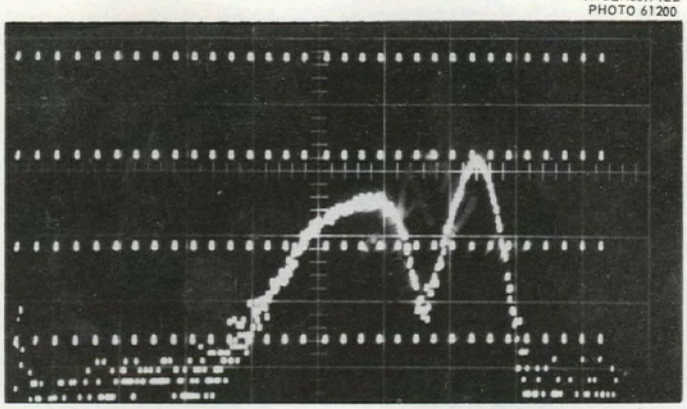

a. Reference Spectrum

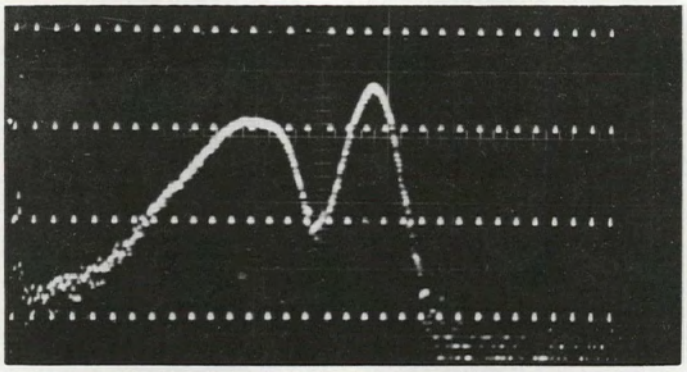

b. Spectrum Delayed 100.9 nsecs with Respect to Figure 17a.

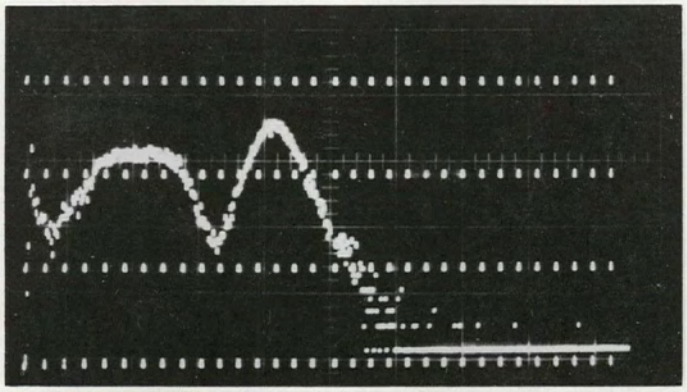

c. Spectrum Delayed 204.7 nsecs with Respect to Figure 17a.

Figure 17. Time-of-Flight Spectrum for $Pu^{239}$

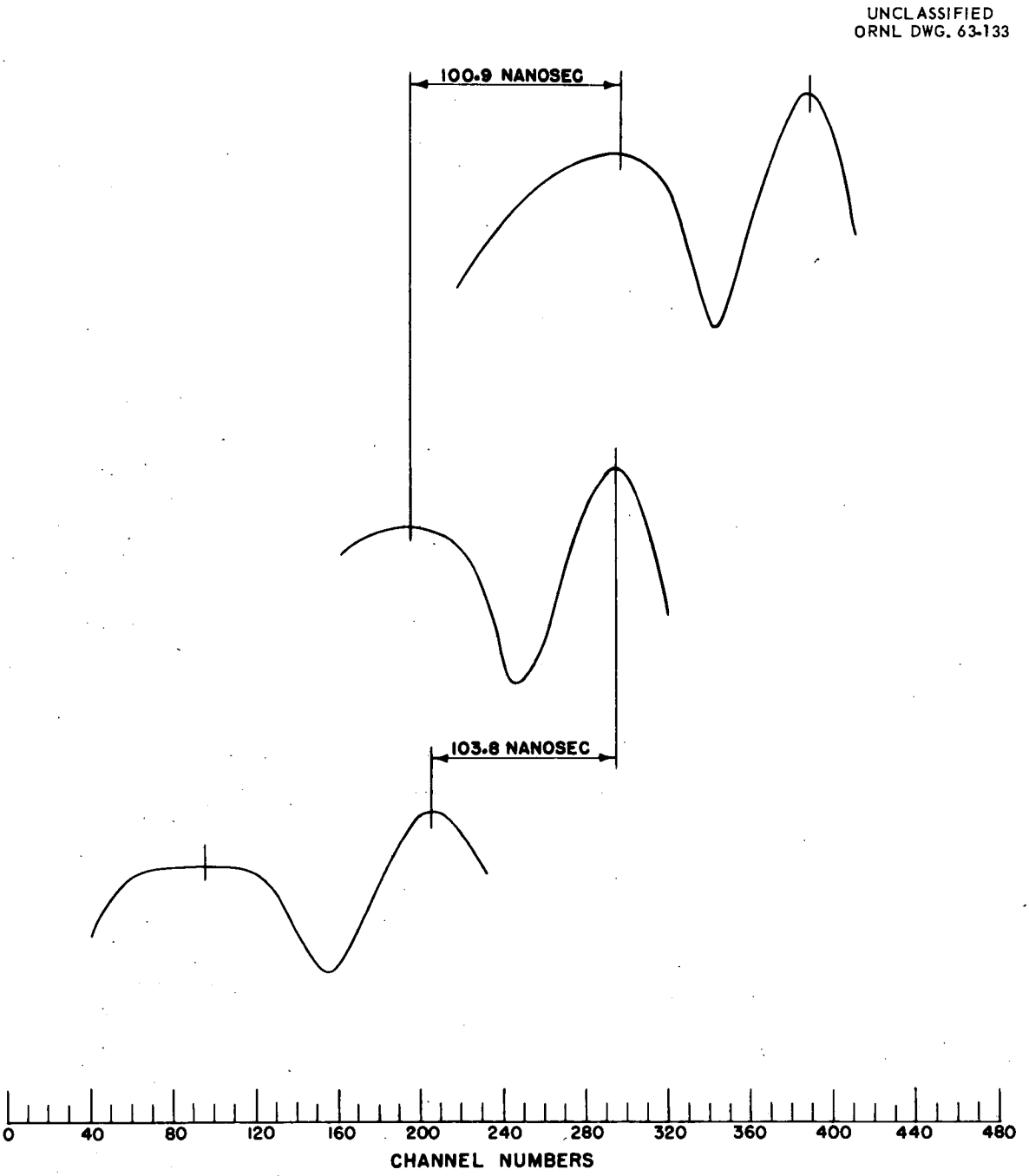


Figure 18. Digital Plot of Figures 17a, b, and c to Establish the Validity of the ART Effect. The Time Delay Between the Light and Heavy Fragment Peaks in (a) is 96.48 nsecs (Milton and Fraser[34]).

UNCLASSIFIED
PHOTO 61199

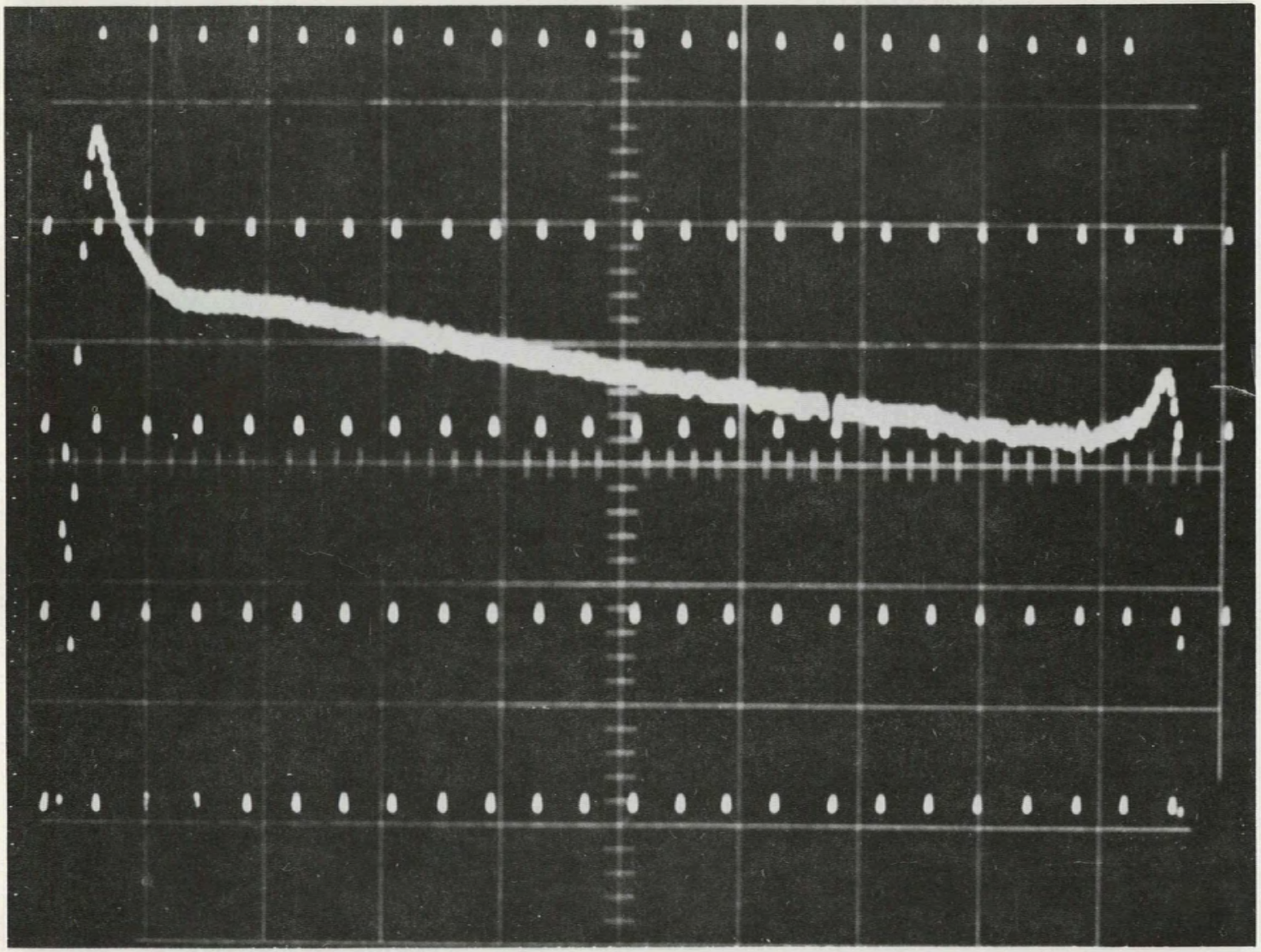

Figure 19. Differential Linearity of the 0-2 Side of the TPHC.

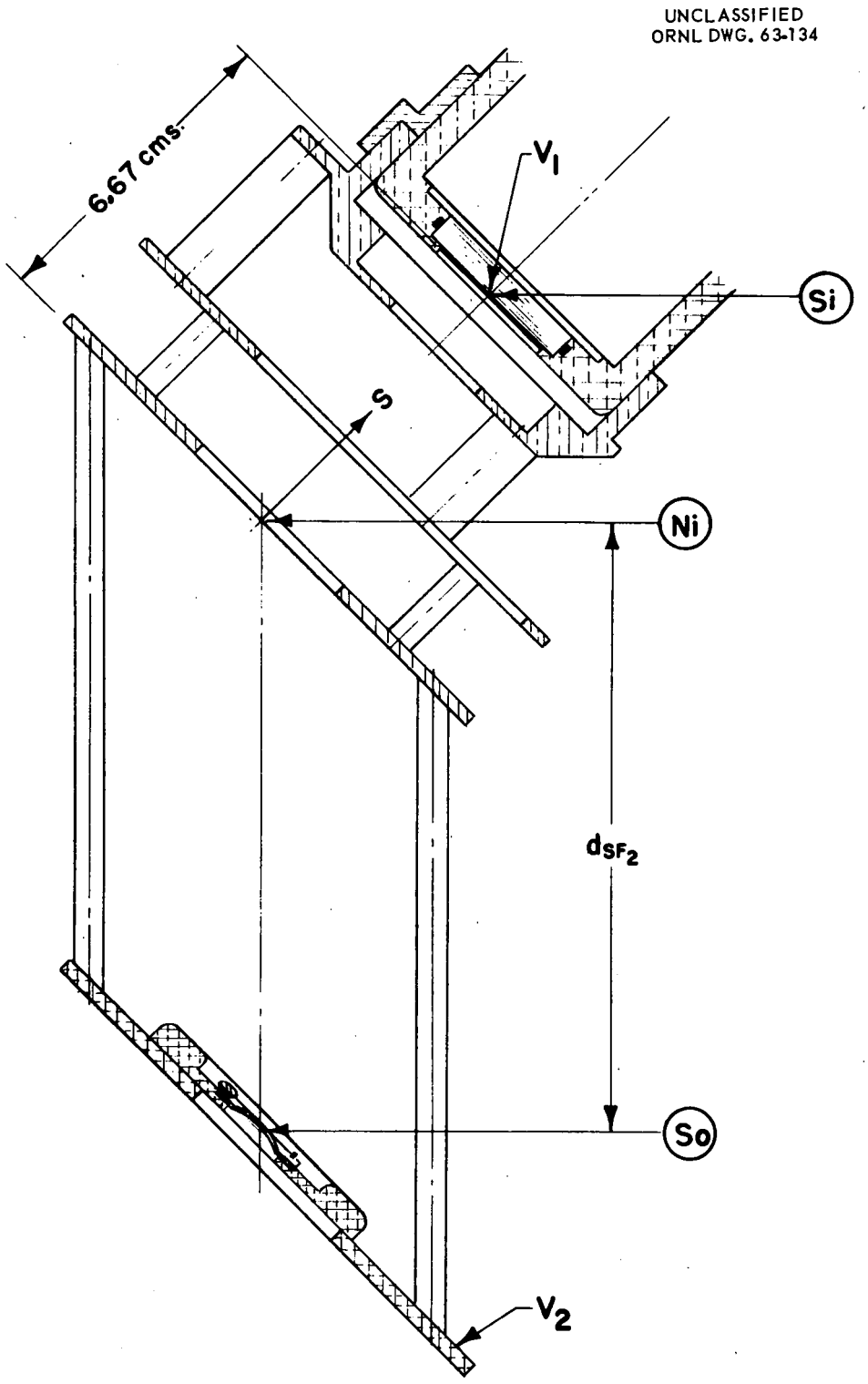


Figure 20. Einzel Lens of the Zero Time Detector.

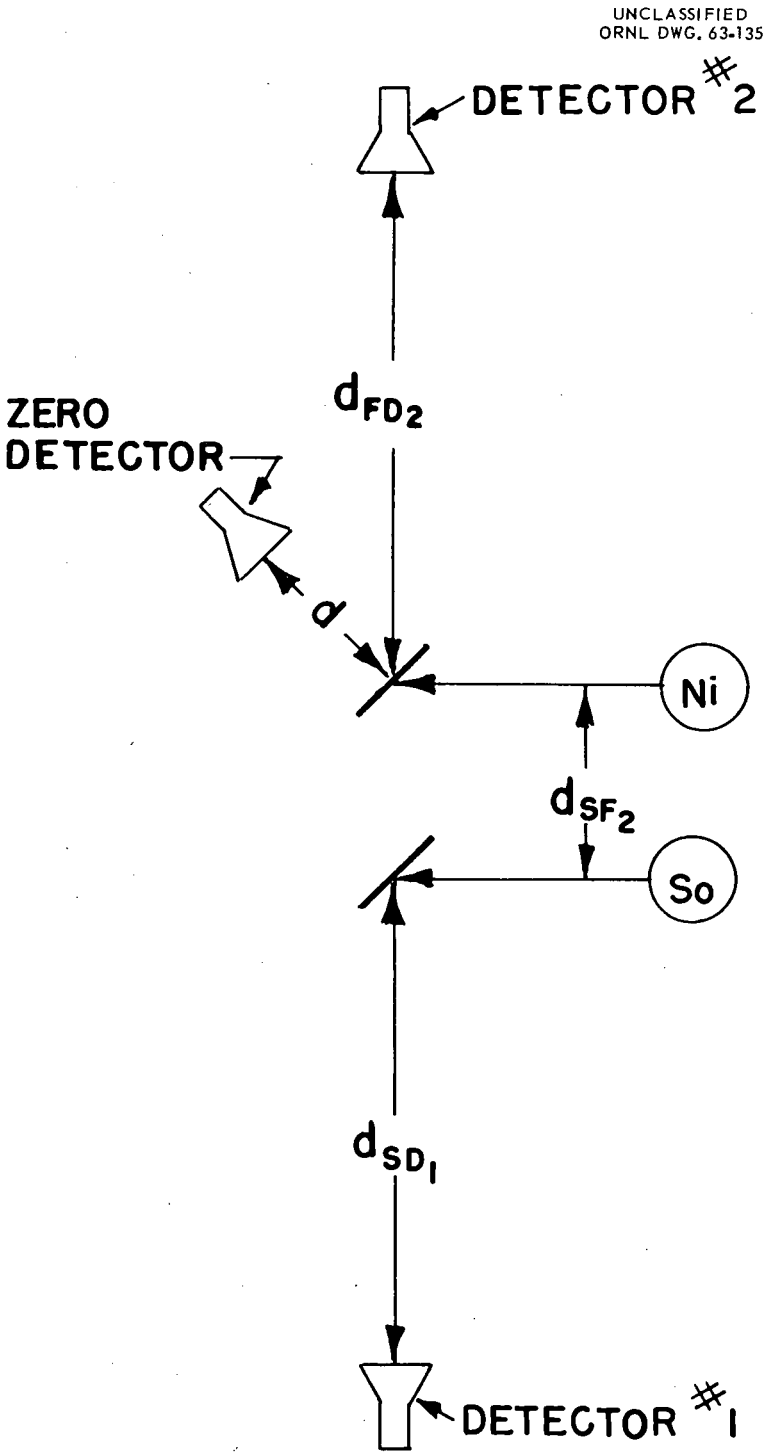


Figure 21. Salient Parameters for Determining the Correlated Fission-Fragment Velocities from the Measurement of Correlated Fission-Fragment Flight Times.

UNCLASSIFIED
PHOTO 61197

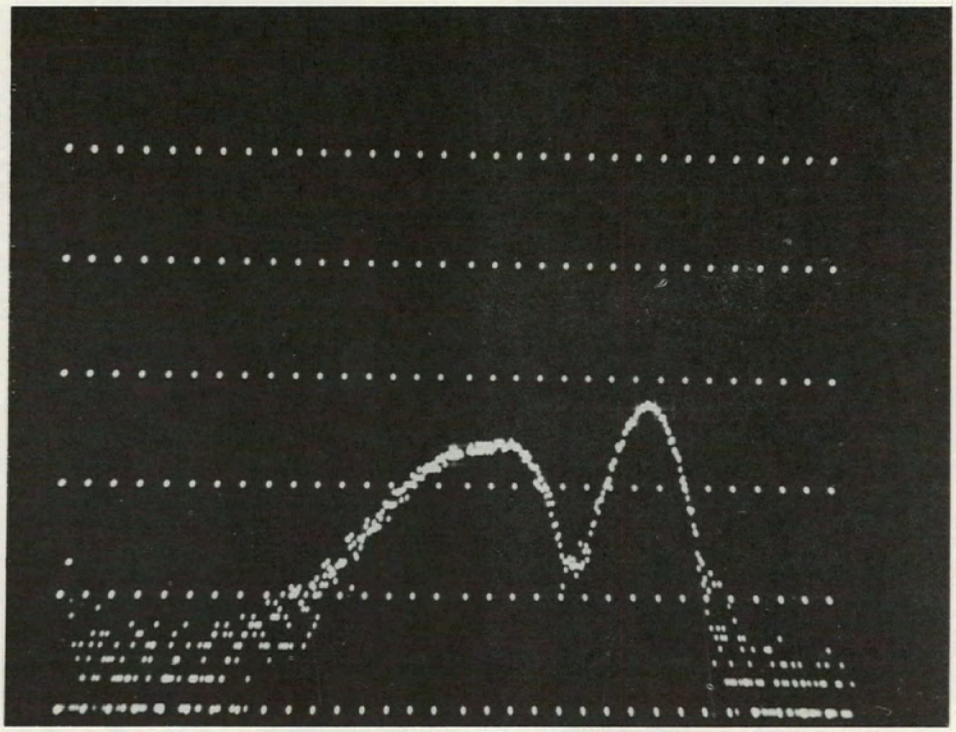

a. A O-2 Time-of-Flight Spectrum (Raw Data).

UNCLASSIFIED
PHOTO 61198

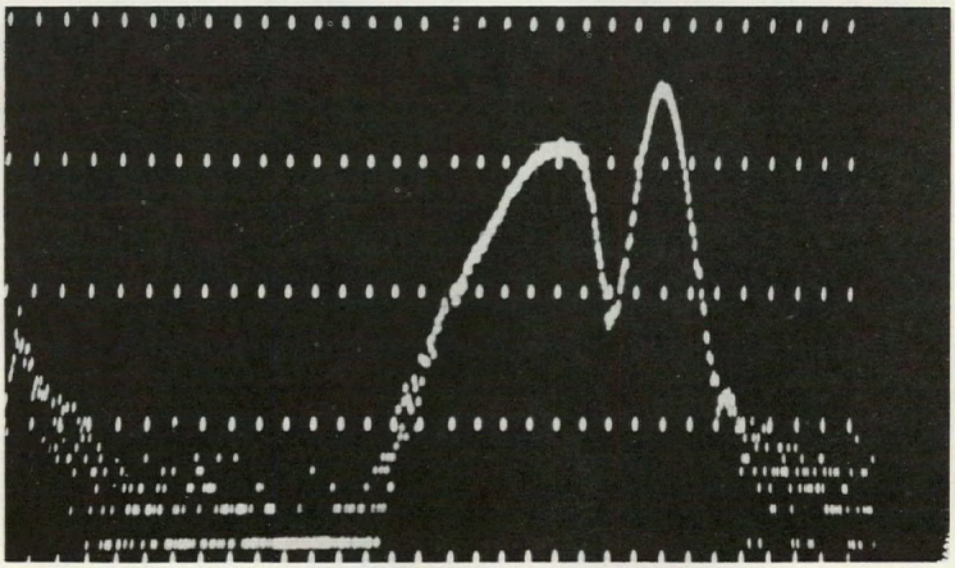

b. A O-1 Time-of-Flight Spectrum (Raw Data).

Figure 22. Time-of-Flight Spectra.

TABLE I

COMBINED EXPERIMENTAL VALUES OF FIVE OBSERVERS IN DETERMINING THE PULSE REPETITION RATE FOR THE TIME DELAY OF THE ZERO-TIME CABLE

| Repetition rate (P.P.S.) | Average repetition rate (P.P.S.) | Maximum deviation (P.P.S.) | Corrected average repetition rate (P.P.S.) | Standard deviation in mean (P.P.S.) | Time delay (nsec) |
|---|---|---|---|---|---|
| 788,733 | 788,733 | ± 300 | $(788.7 \pm 0.3) \times 10^3$ | 30.45 | 633.95 ± 0.025 |
| 788,665 | | | | | |
| 788,781 | | | | | |
| 788,578 | | | | | |
| 788,738 | | | | | |
| 788,672 | | | | | |
| 788,580 | | | | | |
| 788,990 | | | | | |
| 788,878 | | | | | |
| 788,677 | | | | | |

ORNL-3486
UC-34 — Physics
TID-4500 (21st ed.)

## INTERNAL DISTRIBUTION

1. Biology Library
2-4. Central Research Library
5. Reactor Division Library
6-7. ORNL — Y-12 Technical Library
Document Reference Section
8-57. Laboratory Records Department
58. Laboratory Records, ORNL R.C.
59. R. Bender
60. R. D. Birkhoff
61. J. L. Blankenship
62. C. J. Borkowski
63. H. R. Brashear
64. J. B. Davidson
65. D. A. Douglas
66. J. F. Emery
67. S. H. Hanauer
68. J. A. Harter
69. F. F. Haywood
70. N. W. Hill
71. W. H. Jordan
72. C. E. Larson
73. T. A. Love
74. J. L. Lovvorn
75. T. H. Mauney
76-100. W. F. Mruk
101. G. D. O'Kelley
102. M. J. Skinner
103. J. A. Swartout
104. J. R. Tallackson
105. J. H. Thorngate
106. A. M. Weinberg

## EXTERNAL DISTRIBUTION

107. E. H. Cooke-Yarborough, AERE, Harwell, England
108. W. E. Deeds, University of Tennessee
109. J. S. Fraser, Atomic Energy of Canada, Ltd., Chalk River, Canada
110. E. Gatti, C.I.S.E., Milan, Italy
111. W. M. Gibson, Bell Laboratories, Murray Hill, New Jersey
112. R. L. Lide, University of Tennessee
113. J. C. D. Milton, Atomic Energy of Canada, Ltd., Chalk River, Canada
114. A. H. Nielson, University of Tennessee
115. J. F. Pierce, University of Tennessee
116. R. D. Present, University of Tennessee
117. J. D. Tilman, University of Tennessee
118. V. B. Bhanot, Physics Department, Panjab University, Chandigarh-3, India
119. Research and Development Division, AEC, ORO
120-682. Given distribution as shown in TID-4500 (21st ed.) under Physics category